

# Study of the Sextans dwarf spheroidal galaxy from the DART Ca II triplet survey<sup>\*</sup>

G. Battaglia,<sup>1†</sup> E. Tolstoy,<sup>2</sup> A. Helmi,<sup>2</sup> M. Irwin,<sup>3</sup> P. Parisi,<sup>4</sup> V. Hill,<sup>5</sup> P. Jablonka<sup>6</sup>

<sup>1</sup>*European Organization for Astronomical Research in the Southern Hemisphere, K. Schwarzschild-Str. 2, 85748 Garching, Germany*

<sup>2</sup>*Kapteyn Astronomical Institute, University of Groningen, P.O.Box 800, 9700 AV Groningen, the Netherlands*

<sup>3</sup>*Institute of Astronomy, Madingley Road, Cambridge CB03 0HA, UK*

<sup>4</sup>*INAF - Istituto di Astrofisica Spaziale e Fisica Cosmica di Bologna, via Gobetti 101, 40129 Bologna*

<sup>5</sup>*Université de Nice Sophia-Antipolis, CNRS, Observatoire de la Côte d'Azur, Laboratoire Cassiopée, B.P. 4229, 06304 Nice cedex 4, France*

<sup>6</sup>*Observatoire de Genève, Laboratoire d'Astrophysique de l'Ecole Polytechnique Fédérale de Lausanne (EPFL), CH-1290 Sauverny, Switzerland*

Accepted 2010 September 17. Received 2010 September 6; in original form 2010 June 25

## ABSTRACT

We use VLT/FLAMES intermediate resolution ( $R \sim 6500$ ) spectra of individual red giant branch stars in the near-infrared Ca II triplet (CaT) region to investigate the wide-area metallicity properties and internal kinematics of the Sextans dwarf spheroidal galaxy (dSph). Our final sample consists of 174 probable members of Sextans with accurate line-of-sight velocities ( $\pm 2 \text{ km s}^{-1}$ ) and CaT  $[\text{Fe}/\text{H}]$  measurements ( $\pm 0.2$  dex). We use the Mg I line at  $8806.8 \text{ \AA}$  as an empirical discriminator for distinguishing between probable members of the dSph (giant stars) and probable Galactic contaminants (dwarf stars).

Sextans shows a similar chemo-dynamical behaviour to other Milky Way dSphs, with its central regions being more metal rich than the outer parts and with the more metal-rich stars displaying colder kinematics than the more metal-poor stars.

Hints of a velocity gradient are found along the projected major axis and along an axis at P.A. =  $191^\circ$ , however a larger and more spatially extended sample may be necessary to pin down the amplitude and direction of this gradient.

We detect a cold kinematic substructure at the centre of Sextans, consistent with being the remnant of a disrupted very metal poor stellar cluster.

We derive the most extended line-of-sight velocity dispersion profile for Sextans, out to a projected radius of  $1.6 \text{ deg}$ . From Jeans modelling of the observed line-of-sight velocity dispersion profile we find that this is consistent with both a cored dark matter halo with large core radius and cuspy halo with low concentration. The mass within the last measured point is in the range  $2\text{--}4 \times 10^8 M_\odot$ , giving very large mass-to-light ratios, from 460 to  $920 (M/L)_{V,\odot}$ .

**Key words:** stars: abundances – galaxies: kinematics and dynamics – galaxies: dwarf – Local Group – Galaxies: individual: Sextans dSph – dark matter

## 1 INTRODUCTION

The Sextans dwarf spheroidal galaxy (dSph) is a satellite of the Milky Way (heliocentric distance of  $86 \text{ kpc}$  from Irwin et al. 1990 and Mateo et al. 1995;  $95.5 \text{ kpc}$  from Lee et al. 2003). Sextans was discovered relatively recently by automatic scanning of APM plates by Irwin et al. (1990).

This is because the Sextans dSph (hereafter, Sextans) is one of the most diffuse and faint dSphs, with a central surface brightness  $\Sigma_0 = 18.2 \pm 0.5 \text{ mag arcmin}^{-2}$  and luminosity  $L = 4.1 \pm 1.9 \times 10^5 L_\odot$  (Irwin & Hatzidimitriou 1995). This, together with its location on the sky ( $l = 243.5^\circ$ ,  $b = +42.3^\circ$  from Mateo 1998), results in a considerable amount of contamination from Milky Way stars. This makes it particularly difficult to explore the 2D structure of Sextans and search for possible asymmetries or other features (Irwin & Hatzidimitriou 1995).

A further difficulty in the study of Sextans is given by

<sup>\*</sup> Based on FLAMES observations collected at the ESO, proposal 171.B-0588.

<sup>†</sup> Corresponding author. E-mail: gbattagl@eso.org

its large extent on the sky ( $r_{\text{core}} = 16.6 \pm 1.2$  arcmin;  $r_{\text{tidal}} = 160.0 \pm 50$  arcmin from Irwin & Hatzidimitriou 1995), which is not well suited to the field of view of most current wide area imagers and spectrographs. Several imaging studies of the central region (at most the inner  $40 \text{ arcmin} \times 40 \text{ arcmin}$ ) of Sextans (Mateo et al. 1991, 1995; Bellazzini et al. 2001; Harbeck et al. 2001; Lee et al. 2003) have shown that the majority of its stars are ancient ( $>10$  Gyr old), as evidenced by the presence of horizontal branch (HB) and RR Lyrae stars. A significant population of stars have also been found on the main sequence (MS), above the oldest turn-off. It was suggested that these may be MS stars as young as 2 Gyr (e.g. Mateo et al. 1991). However, deep Suprime-Cam V and I photometry at Subaru (Okamoto et al. 2008) shows that their spatial distribution is very similar to old ( $>10$  Gyr) MS stars below the oldest turn-off, indicating that these are likely to be old blue stragglers (BS) stars ( $>10$  Gyr) rather than young MS stars (see also Lee et al. 2003).

In common with other dSphs, Sextans presents spatial variations of its stellar population mix, with the red horizontal branch (RHB) stars more centrally concentrated than the blue horizontal branch (BHB) stars (Bellazzini et al. 2001; Harbeck et al. 2001; Lee et al. 2003; Kleyna et al. 2004). By estimating the luminosity difference between the HB and the main-sequence turn-off out to the nominal tidal radius of Sextans, Okamoto et al. (2008) estimate an age difference of at least 3 Gyr between the outer parts (with age  $\sim 14$  Gyr) and the central parts (with age  $\sim 10$  Gyr). The younger stars are more centrally concentrated than the older ones, consistent with the different distribution of RHB and BHB stars. The other populations, red giant branch (RGB), BS and MS stars, have a spatial distribution intermediate to the one of RHB and BHB stars: this indicates that their spatial distribution can be thought of as a combination of the stellar distribution of RHB and BHB stars, i.e. RGB, BS and MS are likely to represent both components.

No determinations have yet been made of the large scale metallicity properties in Sextans. Spectroscopic estimates of the mean metallicity ( $[\text{Fe}/\text{H}]$ ) of Sextans are available from Ca II triplet (CaT) observations of individual red giant branch (RGB) stars in the central regions ( $<20$  arcmin) of the galaxy (Da Costa et al. 1991,  $\langle [\text{Fe}/\text{H}] \rangle = -1.7 \pm 0.25$  dex, 6 stars; Suntzeff et al. 1993,  $-2.05 \pm 0.04$  dex, 43 stars), which also revealed an internal  $[\text{Fe}/\text{H}]$  spread. High resolution spectroscopic observations of 5 RGB stars in Sextans by Shetrone et al. (2001) confirmed both the average  $[\text{Fe}/\text{H}]$  found in the CaT studies, and the large range of observed metallicities ( $\Delta[\text{Fe}/\text{H}] = 1.4$  dex). The derivation of the mean  $[\text{Fe}/\text{H}]$  and spread in Sextans by Geisler & Sarajedini (1996) from Washington photometry is also in agreement with the spectroscopic studies. Recently Aoki et al. (2009) and Tafelmayer et al. (2010) follow-up at high spectral resolution 6 and 2 stars in Sextans, respectively, confirming the presence of stars with  $[\text{Fe}/\text{H}]$  down to  $-3.1$ .

Studies on the internal kinematics of Sextans have shown that, in common with the other dSphs, this galaxy exhibits a much larger velocity dispersion than what is expected from the gravitational contribution of its luminous matter, hinting at the presence of large amounts of dark matter (Suntzeff et al. 1993; Hargreaves et al. 1994; Kleyna et al. 2004; Walker et al. 2006). The latest estimate (Walker et al. 2007) based on a velocity dispersion profile

from 504 members gives a mass of  $5.4 \times 10^7 M_{\odot}$  within the last measured point at  $\sim 65$  arcmin (equivalent to  $\sim 4$  core radii,  $\sim 0.4$  tidal radii), i.e. a mass-to-light (M/L) ratio of 130  $(M/L)_{\odot}$ . Strigari et al. (2007) used a sample of 294 members from Walker et al. (2006) and estimated a mass of  $0.9^{+0.4}_{-0.3} \times 10^7 M_{\odot}$  within 0.6 kpc ( $13^{+11}_{-5.8} \times 10^7 M_{\odot}$  extrapolated to 4 kpc), which corresponds to an  $M/L = 260 (M/L)_{\odot}$ . Although the mass estimates are not directly comparable as they refer to different distances from the Sextans centre, they all point to mass-to-light ratios so large as to require considerable amounts of dark matter, if the hypothesis of dynamical equilibrium holds. These spectroscopic samples do not reach the nominal tidal radius and therefore the masses determined are likely to be lower limits.

With its unusually large extent on the sky and large tidal-to-core radius ratio ( $r_{\text{tidal}}/r_{\text{core}} \sim 9.6$  as compared to ratios between 3 and 6 for most of the other classical dSphs, see Irwin & Hatzidimitriou 1995), Sextans seems a natural candidate for tidal disruption. However, no clear signs of disruption such as tidal tails and S-shaped contours have been found in Sextans. This may however just be a consequence of the observational challenge of detecting such signs in a low surface brightness and heavily contaminated object like Sextans, or that such signs are not necessarily expected in tidally disrupted galaxies, as some N-body simulations show (see e.g. Muñoz et al. 2008). A small velocity gradient has been detected approximately along the projected minor axis of this galaxy by Walker et al. (2008). However, given that no proper motions have been directly measured for Sextans, it is unclear whether this gradient is a sign of tidal disruption as predicted, for example, in the models of Oh et al. (1995), due to geometrical effects (Strigari 2010) or an intrinsic gradient.

In this paper we use a spectroscopic sample of line-of-sight velocities and  $[\text{Fe}/\text{H}]$  measurements for 174 RGB stars probable members of Sextans, obtained at VLT/FLAMES, to analyse both the wide-field metallicity properties and the internal kinematics of this galaxy. Our sample extends out to 6 core radii (0.7 times the nominal tidal radius). The structure of the paper is the following. In Sect. 2 we describe the observations, the data reduction technique and the adopted metallicity scale. In Sect. 3 we deal with the issue of separating Galactic contaminants from Sextans members and we use the Mg I line as an empirical discriminator between dwarf and giant stars. In Sect. 4 we present the results from our survey regarding the wide-area metallicity and kinematic properties of Sextans as well as the presence of kinematic substructures. Finally, we perform a mass determination in Sect. 5 and present discussion and conclusions in Sects. 6 and 7.

## 2 OBSERVATIONS AND DATA REDUCTION

The spectroscopic observations were carried out at VLT/FLAMES between 2003-2004, with the exception of one pointing which was re-observed in May 2008, during the commissioning of the upgraded GIRAFFE spectrograph CCD.

For the selection of our spectroscopic targets we used photometric data from INT/WFC covering approximately an area of  $2 \text{ deg} \times 2 \text{ deg}$  centred on the coordinates of the op-

tical centre galaxy and ESO/WFI photometry for 12 pointings spread over the outer regions of the system. The imaging data were reduced following standard procedures, for details see references in Battaglia et al. (2006). In this work these photometric data are used exclusively to select spectroscopic targets.

We selected targets classified as stellar in our photometry and with a position on the colour-magnitude diagram (CMD) consistent with an RGB star, but with a wide colour range to avoid biasing our sample in age or in metallicity.

We used VLT/FLAMES feeding the GIRAFFE spectrograph in Medusa mode, that allows the simultaneous allocation of 132 fibres (including sky fibres) over a 25' diameter field of view (Pasquini et al. 2002). We used the GIRAFFE low resolution grating LR8 (resolving power  $R \sim 6500$ ), covering the wavelength range from 8206 Å to 9400 Å. This allows the measurement of equivalent widths (EW) from the near-infrared CaT lines at 8498, 8542, and 8662 Å and also enables the derivation of velocities accurate to a few km/s. The spectra used in this work are from 16 different fields in Sextans obtained with this set-up (see Tab. 2 for the observations journal). These data were reduced using the GIRAFFE pipeline (Geneva Observatory; Blecha et al. 2003).

The sky-subtraction and extraction of the velocities and EWs of CaT lines were carried out using our own software developed by M. Irwin. For the details see Battaglia et al. (2008). Here we just note that we estimate the CaT EW in two ways. The first consists in simply summing the flux contained in a region 15 Å wide centred on each CaT line (hereafter, integral fit). To derive the second estimate we fit individual unconstrained Gaussian functions to each CaT line over the same wavelength region (hereafter, Gaussian fit). The combined EWs for CaT lines #2 and #3 ( $\lambda_{8542}$ ,  $\lambda_{8662}$ ) for both the integral and Gaussian fits are then compared and used to compute an overall correction to the Gaussian fit. This is necessary since the observed CaT lines have non-Gaussian wings which are progressively more visible as the EW increases.

Beside the EW of the CaT lines, we also measure the EW of a Mg I line at 8806.8 Å. The EW of this line is estimated using the values from the integrated fit, summing the flux contained in a region 6 Å wide centred on the Mg I line. The EW of this line will be used as a discriminant between Sextans stars and Milky Way contaminants as described in Sect. 3.2.

We observed a total of 1294 targets, which include 103 stars with double measurements, 70 with 3 measurements, 5 with 4 measurements. The number of distinct targets is 1036.

As described in our previous studies using the same instrument and set-up we ensured a high reliability for the data used in our analysis by excluding those stars with S/N per Å  $< 10$  and velocity errors larger than 5 km s<sup>-1</sup> (e.g. Battaglia et al. 2008). In order to ensure the reliability of the EW measurements we also required that the summed EW of the two strongest CaT lines should not differ by more than 2 Å between the determination from the integral fit and the Gaussian fit.

Figure 1 shows the distribution of differences in velocity for the stars that have double measurements (103 objects), both without any selection criteria and adopting the above selection criteria for each measurement (59 objects). Fig-

ure 2 refers to the distribution of differences in summed EW from Gaussian fit of CaT lines and integrated flux for the Mg I line. The determination of the summed CaT EW from the integral and Gaussian estimators yield quite similar distributions, and therefore, for consistency with our previous work, hereafter we use the summed CaT EW derived from the Gaussian estimator. For the EW of the Mg I line the integral estimator yields slightly less noisy measurements and therefore we will use this for the Mg I line. The error in the summed CaT EW for the individual measurements is given by  $\sigma_{\Sigma W} = 6/(S/N)$ , while the error in the Mg I EW is well represented by  $2.8/(S/N)$ .

In the following, when calculating the velocity, summed CaT EW and all the other properties of the stars with repeated measurements, we use only the individual measurements which meet our S/N and velocity errors criteria (before combining them).

The final sample was carefully checked to weed out any spurious objects (e.g. broken fibres, background galaxies, foreground stars, etc.). We removed 4 objects because they were observed with broken fibres; we found 3 background galaxies and removed 9 objects because the continuum shape or the presence of very broad absorption line was not consistent with what is expected for RGB stars.

Our final sample of acceptable measurements for velocities and CaT EWs consists of 789 stars. We provide a detailed comparison between this data-set and the one from Walker et al. (2009) in the Appendix.

## 2.1 Metallicity scale

We use the CaT EWs to derive metallicities ( $[\text{Fe}/\text{H}]$ ) for the target stars.

The near-infrared CaT lines have been extensively used in the literature as empirical estimators of the  $[\text{Fe}/\text{H}]$  abundance of individual RGB stars observed at intermediate spectral resolution.

This method has been empirically calibrated for stellar clusters and proven reliable over the range  $-2.1 \lesssim [\text{Fe}/\text{H}] \lesssim -0.2$  and  $2.5 \lesssim \text{age [Gyr]} \lesssim 13$  (e.g. Rutledge et al. 1997; Cole et al. 2004) on the Carretta & Gratton (1997) metallicity scale. Battaglia et al. (2008) tested the validity of the method for composite stellar populations, observing the same 129 individual stars in the Sculptor and Fornax dSphs both at intermediate and high resolution, and showed that the CaT EW-  $[\text{Fe}/\text{H}]$  relation can be applied to composite stellar populations over the explored range  $-2.5 \lesssim [\text{Fe}/\text{H}] \lesssim -0.5$ .

Starkenburg et al. (2010) carried out a synthetic spectral analysis of the CaT lines down to  $[\text{Fe}/\text{H}] = -4$  in order to understand their theoretical behaviour as a function of physical parameters such as metallicity, gravity, effective temperature and possible biases in the low metallicity range. The authors find that the a simple linear relation no longer holds approximately below  $[\text{Fe}/\text{H}] \lesssim -2.5$ . This behaviour is mostly a reflection of the change of the CaT lines from wing-dominated at high metallicity to core-dominated at low metallicity.

The authors provide a revised relation, which holds over the much larger range  $-4.0 \lesssim [\text{Fe}/\text{H}] \lesssim -0.5$ :

$$[\text{Fe}/\text{H}] = -2.87 + 0.195 \times (V - V_{\text{HB}}) + 0.458 \times \Sigma W +$$

$$-0.913 \times \Sigma W^{-1.5} + 0.0155 \times \Sigma W \times (V - V_{\text{HB}}) \quad (1)$$

In the above  $\Sigma W$  is the summed EW of the two strongest CaT lines, i.e.  $\Sigma W = EW_2 + EW_3$ ,  $V$  is the apparent magnitude in V-band of the star and  $V_{\text{HB}}$  is the apparent magnitude in V-band of the horizontal branch of the galaxy. For Sextans we use  $V_{\text{HB}} = 20.35$  from Irwin & Hatzidimitriou (1995), which is also consistent with our photometry.

Using our sample of 789 stars along the line-of-sight to Sextans, we find that the  $[\text{Fe}/\text{H}]$  values derived using Eq. (16) in Battaglia et al. (2008) and Eq. (1) compare very well down to  $[\text{Fe}/\text{H}] = -2$ ; at lower metallicities, Eq. (16) from Battaglia et al. (2008) provides on average a larger  $[\text{Fe}/\text{H}]$  value than the revised calibration given by Eq. (1), e.g. a  $[\text{Fe}/\text{H}] \sim -2.4$  with the old calibration corresponds to approximately  $[\text{Fe}/\text{H}] \sim -2.6$  with the revised one and  $[\text{Fe}/\text{H}] \sim -2.6$  to about  $[\text{Fe}/\text{H}] \sim -3.0$ .

In the following we will use Eq. (1) for our CaT  $[\text{Fe}/\text{H}]$  determinations. In order to derive the errors in  $[\text{Fe}/\text{H}]$ , we follow the approach of Starkenburg et al. (2010), i.e. we consider that the error due to the photometry is negligible with respect to the error in the determination of the CaT EW and we input in Eq. (1) the values of  $\Sigma W - 1\sigma_{\Sigma W}$  and  $\Sigma W + 1\sigma_{\Sigma W}$  and derive the corresponding  $1\sigma$  lower and upper limit in  $[\text{Fe}/\text{H}]$ . This reflects the fact that the relation is not linear and therefore symmetric errors in the EW determination can translate into asymmetric errors in  $[\text{Fe}/\text{H}]$ .

### 3 MEMBERSHIP

Given the low surface brightness of Sextans and its location on the sky, the RGB locus of Sextans is heavily contaminated by Milky Way stars which are located along the line-of-sight to Sextans. In order to study the metallicity and kinematic properties of Sextans it is important that we first weed out these Galactic interlopers from our sample. These interlopers will be mostly foreground MW stars. Given the Galactic coordinates of Sextans, the Besançon model (Robin et al. 2003) predicts that the majority of interlopers along the line-of-sight to Sextans is made of dwarf stars, mostly from the thin and thick disk, and by smaller fraction by sub-giants and giant stars.

Ideally one would like a method allowing a direct discrimination between members of the dSph (which have been selected to be RGB stars) from non-members (mostly dwarf stars) on the basis of, for example, spectral features indicating physical characteristics, such as in this case gravity. However, no such spectral features have been identified in previous studies using a similar spectral range and set-up. The common approach is therefore statistical.

The simplest way of discerning between members and non-members is to consider the line-of-sight velocity distribution of the observed targets (see Figure 3 for the distribution of heliocentric velocities for our VLT/FLAMES targets) and iteratively apply a  $k\sigma$  cut around the systemic velocity of the galaxy, where  $\sigma$  is the internal line-of-sight velocity dispersion of the galaxy. The  $k\sigma$  cut in common use is the  $3\sigma$  cut, justified by the close to Gaussian line-of-sight velocity distribution observed for dSphs.

We first follow this approach and then refine our selection using further criteria.

#### 3.1 3- $\sigma$ clipping

We first identify the peak of the velocity distribution and derive the weighted average velocity and dispersion for the stars with a velocity within  $4\sigma$  of the peak, using as a first guess a broad dispersion of  $\sigma = 15 \text{ km s}^{-1}$ . We then repeat the procedure restricting the range of selection to  $3\sigma$ . We then apply to the distribution of line-of-sight velocities for the stars within the  $3\sigma$  range the maximum likelihood method outlined in Hargreaves et al. (1994). This results in a systemic velocity  $v_{\text{sys, hel}} = 226.3 \pm 0.6 \text{ km s}^{-1}$  and a global dispersion  $\sigma_{\text{hel}} = 8.8 \pm 0.4 \text{ km s}^{-1}$  for 182 probable members. The systemic velocity derived is in very good agreement with the value of  $v_{\text{sys, hel}} = 225.8 \pm 0.5 \text{ km s}^{-1}$  from Walker et al. (2006); for the global dispersion they quote values from 3 sample sizes:  $N=276 \sigma_{\text{hel}} = 7.1 \pm 0.3 \text{ km s}^{-1}$ ;  $N=294 \sigma_{\text{hel}} = 8.9 \pm 0.4 \text{ km s}^{-1}$ ;  $N=303 \sigma_{\text{hel}} = 10.3 \pm 0.5 \text{ km s}^{-1}$ . Our determination is in very good agreement with their determination from the  $N=294$  sample. We find a good agreement also with the values derived by Hargreaves et al. (1994) ( $v_{\text{sys, hel}} = 224.4 \pm 1.6 \text{ km s}^{-1}$ ,  $\sigma_{\text{hel}} = 7.0^{+1.3}_{-1.0} \text{ km s}^{-1}$  from 21 members), and consistent values also to the study of Suntzeff et al. (1993) ( $v_{\text{sys, hel}} = 227.9 \pm 1.8 \text{ km s}^{-1}$ ;  $\sigma_{\text{hel}} = 6.2 \pm 0.9 \text{ km s}^{-1}$  based on 33 stars).

Given the large extent on the sky of Sextans, the Solar motion and Local Standard of Rest (LSR) will contribute a component along the line-of-sight to the object, which may introduce spurious velocity gradients and affect the derivation of quantities such as internal rotation for example. In order to remove this effect we transform the heliocentric line-of-sight velocities into line-of-sight velocities in a frame at rest with respect to the Galactic centre ( $v_{\text{GSR}}$  where GSR stands for Galactic standard of rest). For this we use the formula in Binney & Tremaine (1987), using a LSR velocity  $v_{\text{LSR}} = 220 \text{ km s}^{-1}$  at the Solar radius ( $R_{\odot} = 8 \text{ kpc}$ ) and a Solar motion of  $(U, V, W) = (10, 5.25, 7.17) \text{ km s}^{-1}$  (Dehnen & Binney 1998), where  $U$  is radially inward,  $V$  positive in the direction of Galactic rotation and  $W$  towards the North Galactic Pole.

We repeat the determination of the systemic velocity and global dispersion using the GSR velocities, and we obtain  $v_{\text{sys, GSR}} = 78.6 \pm 0.7 \text{ km s}^{-1}$  and  $\sigma_{\text{GSR}} = 8.8 \pm 0.5 \text{ km s}^{-1}$  for 182 probable members. Here after we will use the GSR velocities, except when comparing the individual line-of-sight velocities from this study those from other studies to ease the comparison.

#### 3.2 Use of the Mg I line at 8806.8 Å as a dwarf/giant discriminator

Figure 4 shows the distribution of  $[\text{Fe}/\text{H}]$  measurements for targets along the line-of-sight to Sextans against their line-of-sight velocity in the GSR system<sup>1</sup>. Around the systemic velocity of Sextans  $\pm 3\sigma_{\text{GSR}}$  one can distinguish the stars that are probable members of the galaxy, from those likely

<sup>1</sup> Note that the CaT relation relies on the assumption that all the stars can be considered at the same distance. While this is a reasonable assumption for the stars belonging to the Sextans dSph, this is most likely not the case for the foreground/background MW stars. Therefore, the  $[\text{Fe}/\text{H}]$  values for the stars which are probable non-members cannot be considered as meaningful.

to be foreground/background MW stars. From Fig. 4 it is clear that a simple kinematic selection like the  $3\sigma$  clipping is able to remove the majority of the MW contaminants but that a small fraction may still be present in the  $3\sigma$  region of membership selection. The fraction of contaminants appears to change with the  $[\text{Fe}/\text{H}]$  value derived from the CaT lines: at  $[\text{Fe}/\text{H}] \lesssim -2.0$  no considerable contamination is expected, while at larger metallicities Sextans stars are more likely to be contaminated by Galactic stars whose velocity falls in the  $3\sigma$  membership selection region.

Here we attempt a new empirical approach to refine our membership determination, using the Mg I line at  $8806.8\text{\AA}$  as a further possible discriminator between MW and Sextans members.

We first select the stars that have a high probability of membership to Sextans by restricting the velocity range of selection to  $2\sigma_{\text{GSR}}$  just for the purpose of this analysis; the highly likely non-members are chosen to be the ones with GSR velocity more than  $4\sigma_{\text{GSR}}$  away from Sextans systemic velocity. Given the small EW of the Mg I line, in general less than  $1\text{\AA}$ , only spectra with  $\text{S/N}/\text{\AA} > 20$  are used to explore possible trends without being affected considerably by the noise. In order to explore the behaviour of the Mg I line with gravity in an empirical way, in Fig. 5 we show the behaviour of the EW of the Mg I line versus the CaT  $\Sigma W$  in bins of V-magnitude, for both high likely members and non-members.

As it is visible in Fig. 5 the loci of Mg I EW are quite distinct for members and non-members: members cluster at EW between  $\sim 0$  and  $0.2\text{\AA}$ , while non-members occupy preferably the region of Mg I EW between  $0.5$  and  $0.9\text{\AA}$ . Some members have negative Mg I EW: this is just a reflection of the lower S/N of those spectra; considering the error-bars these are consistent with Mg I EW close to zero, therefore with the line being hidden in the noise.

It is clear that in general the non-members display a larger Mg I EW with respect to members. Preliminary use of synthetic stellar models suggest that this difference may not be driven exclusively by gravity but also of the different metallicity of the dSph star and MW stars (with the former being below  $[\text{Fe}/\text{H}] < -1$  and the latter peaking around  $-0.5$  to  $\sim 0$ ).

From the figure it appears that the trend of Mg I EW versus CaT  $\Sigma W$  changes slightly among the bins in V-magnitude, which on a first approximation indicates a dependence on the gravity. However, a safe selection is to consider as members the stars with  $\text{Mg I EW} < 0.5\text{\AA}$ . Hereafter we add this constrain to our selection criteria for probable Sextans stars. We have checked that this selection is valid also when exploring the behaviour of the Mg I EW versus CaT  $\Sigma W$  in bins of V–I, as a proxy for effective temperature.

Applying this selection, 6 stars classified as members from the  $3\sigma$  clipping appear to be contaminants (these are indicated as diamonds in Fig. 4).

We will improve on the simple empirical approach presented in this section using synthetic spectral libraries in order to assess the applicability range of this method.

### 3.3 Location on the CMD

Our VLT/FLAMES targets have been chosen to have magnitudes and colours broadly consistent with that expected

for RGB stars. We can now apply the membership criteria of the previous two sections to redefine the RGB locus occupied by probable Sextans members. Figure 6 shows the location on the CMD of the probable members and probable non-members, selected using the criteria of Sects. 3.1 and 3.2. All the probable members are closely located along the RGB ridge. The only evident outlier is found at  $V-I \sim 0.9$  and  $V \sim 17.2$  (see Fig. 6). This star is located at a projected distance  $R \sim 2.2\text{ deg}$ . Given its metallicity of  $[\text{Fe}/\text{H}] = -1.9$ , its location on the CMD appears inconsistent with stellar evolution models; we therefore exclude this star from subsequent analysis.

### 3.4 Final sample of probable members

By adopting all the membership criteria described above, i.e.  $3\sigma$  velocity clipping, Mg I EW and location on the CMD, the final sample of probable members is 174 stars. We have also excluded one star having an error in  $[\text{Fe}/\text{H}] > 1$  dex. Using this sample the systemic velocity and global dispersion in the GSR system are  $v_{\text{sys,GSR}} = 78.4 \pm 0.6\text{ km s}^{-1}$  and  $\sigma_{\text{GSR}} = 8.4 \pm 0.4\text{ km s}^{-1}$ , while in the heliocentric system they are  $v_{\text{sys,hel}} = 226.0 \pm 0.6\text{ km s}^{-1}$  and a global dispersion  $\sigma_{\text{hel}} = 8.4 \pm 0.4\text{ km s}^{-1}$ , all in good agreement with previous determinations. Hereafter we will use this sample for the analysis of the properties of Sextans. The location on the field-of-view of the cleaned up sample and the contaminants is shown in Fig. 7. From this plot the problems in collecting large samples of individual stars in an object like Sextans are clear: it is very extended, therefore many pointings of wide-field area spectrographs like FLAMES are needed, and because of its very low surface brightness, the outermost 3 pointings did not yield any probable members.

## 4 RESULTS

### 4.1 Metallicity properties

Metallicity measurements of large numbers of individual stars are important since they can shed light on the processes that drive galactic chemical enrichment and by measuring the metal abundance in stars over a wide age range and across the galaxy one can recover how the metal content built up in time and how the enrichment proceeded throughout the galaxy.

Figure 8 shows the metallicity distribution of probable members of Sextans as derived from our VLT/FLAMES data (left: as a function of elliptical radius; right: overall distribution). The stars in Sextans cover a wide range of  $[\text{Fe}/\text{H}]$  values, with the majority covering values from about  $-3.2$  to  $-1.4$ , but reaching down to  $-3.8$  and up to  $-0.1$ ; the average value of the distribution is  $[\text{Fe}/\text{H}]_{\text{avg}} = -1.9$ , with a scatter of  $0.6$  dex, and the median value is  $[\text{Fe}/\text{H}]_{\text{med}} = -2.3$ .

The left panel of Fig. 8 clearly shows that the metallicity properties of this galaxy change with the projected radius from the centre: the inner parts of the galaxy are more metal rich than the outer parts. This kind of behaviour is not unique to Sextans but has been detected also in other Milky Way satellites, on the basis of CaT data. However, here in Sextans the behaviour is more enhanced than in the other systems, with a step like behaviour of the metallicity

distribution going from the region at  $R < 0.8$  deg to the region at  $R > 0.8$  deg: while the inner parts ( $R < 0.8$  deg) show a broad distribution, covering the whole range of  $[\text{Fe}/\text{H}]$  values, the stars in the outer parts ( $R > 0.8$  deg) appear to have all  $[\text{Fe}/\text{H}]$  values  $< -2.2$  (except for 2 stars out of 19). The current data appear to suggest a  $[\text{Fe}/\text{H}]$  threshold ( $[\text{Fe}/\text{H}] = -2.2$ ) in the outer parts, but more data would be required to confirm that this result is not due to small number statistics.

It is likely that the two “metal-rich” stars at  $R > 0.8$  deg are contaminants: their  $[\text{Fe}/\text{H}]$  value is very discrepant with respect to the rest of the distribution, with metallicities of about 1 dex above the largest  $[\text{Fe}/\text{H}]$  of the rest of the stars. These stars may be RGB stars belonging to the stellar halo of our Galaxy. Similarly, at  $R \sim 0.5$  deg, one star is present with  $[\text{Fe}/\text{H}] \sim -0.1$ , more than 1 dex larger than the maximum  $[\text{Fe}/\text{H}]$  displayed by all the other probable Sextans members anywhere in the galaxy. Even though it is possible that these 3 stars may belong to the stellar halo of the Milky Way, these objects full-fill all our membership criteria and we have no means to distinguish them in a direct way from genuine Sextans members, therefore we will keep them in the analysis.

As shown in Fig. 9 the metallicity distribution of  $R > 0.8$  deg is well approximated by a Gaussian with best-fitting peak position at  $[\text{Fe}/\text{H}] = -2.73 \pm 0.06$  and dispersion  $0.24 \pm 0.05$  dex (reduced  $\chi^2 = 0.6$ ). The same figure shows that the region at  $R < 0.8$  deg is well represented by a sum of two Gaussians: one having the same shape parameters -modulo the amplitude- as in the outer parts, and the other Gaussian with best-fitting peak position at  $[\text{Fe}/\text{H}] = -2.04 \pm 0.03$  and dispersion  $0.25 \pm 0.03$  dex (reduced  $\chi^2 = 0.7$ ). At  $R < 0.8$  deg these two Gaussians do overlap over a metallicity range and at  $[\text{Fe}/\text{H}] \sim -2.3$  the contribution of the stars belonging to the “metal-rich” component is that of the “metal-poor” stars<sup>2</sup>. We will come back to this point in Sect. 4.3.2.

Figure 9 also shows the presence of 31 stars with CaT  $[\text{Fe}/\text{H}] < -2.8$ , whose presence was not revealed when using the CaT calibration based on globular clusters; 11 of these stars have  $[\text{Fe}/\text{H}] < -3$ , i.e. they could be classified as extremely metal poor stars. The presence of stars of these metallicities excludes the hypothesis that Sextans was formed from a pre-enriched medium of  $[\text{Fe}/\text{H}] > -3$  as Helmi et al. (2006) put forward.

Seven Sextans stars with CaT  $[\text{Fe}/\text{H}] \lesssim -2.7$  have been followed up at high spectral resolution by Aoki et al. (2009) and Tafelmayer et al. (2010), showing that the CaT calibration holds down to these low metallicities.

## 4.2 Velocity gradients

Early studies on dSphs, based on datasets of dozens of line-of-sight velocities in the central regions of these objects, had not yielded statistically significant detections of velocity gradients in these galaxies and therefore dSphs have commonly been regarded as exclusively pressure supported systems.

The gathering of much larger datasets, with hundreds line-of-sight velocities spread throughout the face of dSphs, led to the detection of velocity gradients in several of these objects.

Figure 10 shows a velocity field for Sextans obtained from the probable members of the galaxy. There are hints of the presence of a velocity gradient along the projected major axis of Sextans, but from this plot it is also evident that, given the small number of stars distributed over a large area, more details, such as velocity contours, cannot be reliably obtained.

We analyse the velocity trends of the probable members along different directions across the face of the galaxy. Given the relatively sparse spatial sampling, we explore only 4 directions: along the major and minor axes (P.A. =  $56^\circ, 146^\circ$ , respectively) and along 2 intermediate axes (P.A. =  $101^\circ, 191^\circ$ ). We consider a slit of variable width along those axes and explore the trend of the line-of-sight velocity in the GSR frame as a function of the linear distance from the centre of the galaxy for those stars within the “slit”. We decided not to bin the data, as they are too sparse.

Figure 11 shows the results for a slit width of 0.3 deg. As fiducial functional form for the gradient we use a straight-line, with the intercept fixed to the systemic velocity, and we perform an unweighed fit to the data points referring to the probable members. In order to derive the error in the fitted slope, we create 10000 mock velocity datasets in which the stars are as many as the number of probable members and with the same positions, but the velocities are drawn from Gaussians centred on the measured velocities and with dispersion given by the velocity errors and the global dispersion of Sextans added in quadrature. For each of these mock datasets we repeat the unweighed fit to the velocities along the various axes; the error in the slope is given by the  $1\sigma$  level in the distribution of fitted slopes. For this slit width the detected slopes are:  $8.5 \pm 3.0$  km s<sup>-1</sup> deg<sup>-1</sup> along the major axis,  $-0.8 \pm 4.2$  km s<sup>-1</sup> deg<sup>-1</sup> along the minor axis,  $0.4 \pm 5.3$  km s<sup>-1</sup> deg<sup>-1</sup> along the axis at P.A. =  $101^\circ$  and  $7.5^{+3.4}_{-3.0}$  km s<sup>-1</sup> deg<sup>-1</sup> along the axis at P.A. =  $191^\circ$ .

In order to assess the significance of such detections we repeat the above procedure reshuffling the measured velocities 10000 times, where this should be equivalent to eliminating any coherent motion and therefore simulating a non-rotating dSph with the same overall dispersion as measured for Sextans. We then calculate how many times the mock datasets give amplitudes larger than the measured ones. For a slit width of 0.3 deg the percentages are 0.4%, 58.4%, 46.9% and 0.9% along the major, minor, P.A. =  $101^\circ$  and P.A. =  $191^\circ$  axes, respectively.<sup>3</sup> The only statistically significant detections appear to be the ones along the major axis and along the axis at P.A. =  $191^\circ$ . If these velocity gradients are due to rotation about the minor axis of Sextans, we would expect to detect similar velocity gradients along the P.A. =  $101^\circ$  and P.A. =  $191^\circ$  axes, given that they are

<sup>2</sup> Here the Gaussian fit to the metallicity distribution at different distances from the centre is only meant to highlight the differences in the peak metallicity value between the inner and outer parts.

<sup>3</sup> We checked whether the gradient along the P.A. =  $191^\circ$  axis may be driven by the two points at distance larger than 0.9 deg, by repeating the determination removing these two points. The gradient is still present,  $6.3 \pm 3.7$  km s<sup>-1</sup> deg<sup>-1</sup>, although the significance slightly decreases (the percentage of mock dataset giving as large a gradient increases to 4.5%).

symmetric about the minor axis; however, while the spatial coverage along the P.A.= 191° is quite homogeneous and symmetric about the centre of the galaxy, this is not the case along the P.A.= 101° axis, along which we have data only in the N-W part of the galaxy; it is therefore unclear if the discrepancy in the detection is due to the difference in spatial coverage.

We find that, when increasing the slit width, for example of 0.4 deg, the amplitude of the gradients slightly decreases, which suggests that the kinematics along a certain axis starts to be contaminated by the inclusion of more stars moving differently because placed at different distances from the centre. In this case the percentage of the mock datasets giving amplitudes larger than the measured ones is larger than for a slit width of 0.3 deg, but the gradients along the projected major axis and the P.A.= 191° axis remain statistically significant.

Another concern in the derivation of the velocity gradient is the possible inclusion in the sample of contaminants from the Milky Way, or vice versa the possible exclusion of Sextans stars based on the  $3\sigma$  cut-off. However, none of the two points appear to be an issue in the analysis here carried out as it is visible from Fig. 11 where we also show the non-members falling in the considered slits: from these figures it is clear that the fraction of unidentified contaminants still present in the  $3\sigma$  velocity range is likely to be negligible, and also that we are unlikely to have missed probable members because of the  $3\sigma$  cut-off.

As mentioned already, with the current spatial sampling it is difficult to extract a velocity field and to determine a rotation pattern. We adopt a simple empirical approach and assume that  $v_{\text{rot}} = k * d_{\text{min}}$ , where  $k = 8.5 \text{ km s}^{-1} \text{ deg}^{-1}$  and  $d_{\text{min}}$  is the angular distance of each star from the minor axis along a direction parallel to the major axis (with  $d_{\text{min}}$  positive above the minor axis and negative below the minor axis, the formula gives receding and approaching velocities above and below the minor axis, respectively). To assess how good a representation of the data this is, we subtract the  $v_{\text{rot}}$  from the stars classified as probable members, and re-derive the velocity field and the trends along the various slits. There appears to be a residual pattern in the velocity field from the “rotation-subtracted” velocities; indeed, velocity gradients are still present along the various axes, but they do not appear to be statistically significant. For a slit width of 0.3 deg the detected slopes are:  $-0.1 \pm 3.1 \text{ km s}^{-1} \text{ deg}^{-1}$  along the major axis,  $-1.8^{+4.5}_{-3.9} \text{ km s}^{-1} \text{ deg}^{-1}$  along the minor axis,  $7.1^{+5.2}_{-5.5} \text{ km s}^{-1} \text{ deg}^{-1}$  along the axis at P.A.= 101° and  $1.6 \pm 3.1 \text{ km s}^{-1} \text{ deg}^{-1}$  along the axis at P.A.= 191°. The percentages of mock datasets that give amplitudes larger than the measured ones are large, 48.4%, 66.4%, 9.0% and 30.6% along the major, minor, P.A.= 101° and P.A.= 191° axes, respectively, i.e. the gradients do not appear to be highly statistically significant, meaning that the rotation pattern we assume is a reasonable representation of the data.

It appears that a weak velocity gradient is present in Sextans, but the direction and amplitude of this gradient is difficult to constrain. Note that our determination differs from the determination by Walker et al. (2008), who find a gradient of  $-2.1 \pm 0.8 \text{ km s}^{-1} \text{ deg}^{-1}$  along a P.A.= 120°. Given that the velocities between the two studies compare well (see Appendix), this difference is most likely due to the different coverage and size of the sample, as well as the

methodology used. A larger statistical sample and coverage of the galaxy would help quantifying this better; however, given the low surface brightness and large extent on the sky of Sextans, this may be a challenging task.

### 4.3 Observed velocity dispersion profile

#### 4.3.1 All members

We derive the l.o.s. velocity dispersion profiles for Sextans by binning the velocities of stars at similar radii using the sample of probable members as determined in Sect. 3.4 and deriving the average velocity and dispersion per bin using the procedure described in Hargreaves et al. (1994).

In deriving the l.o.s. velocity dispersion profile we checked for the effect of a number of issues.

First, we check the effect that the number of stars per bin has on the derived l.o.s. velocity dispersion profile by fixing the number of stars per bin to a constant value of  $N=20,25,30$  and  $35$  (except for the last bin, which is allowed to have a lower number of points). We find that, even though the shape and amplitude of the l.o.s. velocity dispersion profiles are consistent within the error-bars among all the cases, the binning with  $N=35$  stars is the most reliable one because it produces less oscillations in the trend of average velocities per bin, and that these velocities are consistent with the systemic velocity.

We then explore the effect of binning the data in elliptical annuli (of constant ellipticity and position angle ( $e = 0.35$  and P.A.= 56°) and circular annuli, using a constant number of  $N=35$  stars per bin. In fact, one uses stars with a non-spherical spatial distribution as kinematic tracers of an underlying distribution which may be spherical (as well as oblate, prolate or even triaxial). We also use a constant number of  $N=35$  stars per bin when exploring the effect of subtracting the detected velocity gradient onto the determination of the velocity dispersion profile (hereafter we refer to the profile derived from the individual velocities from which the velocity gradient has been subtracted as the “rotation subtracted” profile). These results are shown in Fig. 12 (left): the l.o.s. velocity dispersion profiles derived from the elliptical and circular binning, when subtracting or not rotation, all agree with each others within the error-bars. In the following we adopt the rotation subtracted velocities and the elliptical binning.

The effect of using bins of variable width which increases with projected radius, instead than using a constant number of stars per bin, is shown in the right-hand panel of Fig. 12. We explored 3 different binnings, which are labelled as “Binning1”, “Binning2” and “Binning3” in the right-hand side panel of Fig. 12). All these choices of binning are compatible with the trend shown when keeping the number of probable members per bin constant. In the following, When deriving the mass profile of Sextans we will use the l.o.s. velocity dispersion profile from “Binning2”; however, the effects of a different binning on the mass determination will also be considered, by checking the results obtained when using the profile from “Binning3”. We will not use “Binning1” for the analysis because it represents the case where the average velocity per bin differs the most from the systemic.

The l.o.s. velocity dispersion profile of Sextans appears

to slightly increase with radius although, given the large size of the error-bars in the last bins, it is also compatible with remaining constant.

To compare the l.o.s. velocity dispersion profile published by Walker et al. (2007) and ours we should consider the case of the circular binning, with no velocity gradient subtracted: in this case our profile remains approximately constant around  $8 \text{ km s}^{-1}$ , consistent with the determination by Walker et al. (2007).

#### 4.3.2 “Metal-rich” and “Metal-poor” stars

In previous work, we have combined the information on the spatial location, metallicity and velocity of individual stars in dSphs. This allowed us to explore links between the metallicity and the kinematics of stars in the Sculptor and Fornax dSphs (T04 and B06, respectively), and shown that in these systems metal-rich stars - centrally concentrated - have a smaller velocity dispersion than metal-poor stars - which in turn have a more extended spatial distribution. The metallicity chosen to illustrate this different kinematic behaviour between the colder and hotter stellar components is somewhat subjective, but it is chosen on the basis of considerations on the metallicity distribution in order to minimize contamination between the two metallicity components.

As seen in Sect. 4.1 at  $R < 0.8 \text{ deg}$ , the region where the whole range of metallicities is present, the metallicity distribution of Sextans is well-approximated with the sum of two Gaussians, a “metal-rich” and a “metal-poor” one, which cross at  $[\text{Fe}/\text{H}] \sim -2.3$ . Therefore to minimize contamination between these two components, we exclude the range  $-2.4 < [\text{Fe}/\text{H}] < -2.2$  and we derive the trend of mean velocity and dispersion for the stars more metal-rich than  $[\text{Fe}/\text{H}] = -2.2$  and more metal-poor than  $[\text{Fe}/\text{H}] = -2.4$  over different spatial bins.

Figure 13 shows that also in Sextans “metal-rich” and “metal-poor” stars display a different behaviour (akin to our findings in the Fornax and Sculptor dSphs), with the former population in general kinematically colder than the latter. The profile of the metal-rich stars appears to be slightly declining, while for the metal-poor stars it is everywhere constant (except in the first bin, see next section) and extends further than the profile for the MR stars, as a consequence of the larger spatial extent of the metal-poor stars. It remains to be proven if the different spatial extent of the stellar population analysed is the only factor that causes the different kinematics, or if one needs to take into account also different orbital properties for the different stellar populations. Also, the outer bin for the “metal-rich” stars suffers from low number statistics and would certainly benefit from a larger sample of stars with  $[\text{Fe}/\text{H}] > -2.2$ .

#### 4.4 Substructures

Kleyna et al. (2004) detected a kinematically cold substructure, with dispersion close to zero, from 7 stars with radial velocity measurements in the inner 5 arcmin of Sextans. One of the hypothesis that they put forward is that the stars giving raise to this kinematic feature may belong to the remnant of a disrupted stellar cluster which spiraled into Sextans centre. The authors note that this hypothesis can

account for the sharp central rise in the light distribution of Sextans (e.g. Irwin & Hatzidimitriou 1995). Also the distribution of blue stragglers in Sextans, with the brighter (i.e. more massive) blue stragglers more centrally concentrated than the fainter ones (Lee et al. 2003) could be explained by this mechanism. The authors estimate a luminosity of  $1.3 \times 10^5 L_{\odot}$  for the disrupted cluster. The existence of this central cold substructure has not been confirmed by subsequent studies such as Walker et al. (2006), who instead find another cold substructure of estimated luminosity  $\sim 10^4 L_{\odot}$  at a different location, i.e. around the core radius of the galaxy.

The inner point in Fig. 13 shows peculiar characteristics for the metal-poor stars: the velocity dispersion is very cold,  $1.4 \pm 1.2 \text{ km s}^{-1}$ , and the average velocity is  $72.5 \pm 1.3 \text{ km s}^{-1}$ , about  $4\sigma$  away from the systemic<sup>4</sup>. In the binning used these values are derived from the 6 innermost metal-poor stars, however from panel (a) of Fig. 13 it can be seen that other 3 MP stars at  $R < 0.22 \text{ deg}$  share very similar velocities to this group of stars; only 1 MP star at  $R < 0.22 \text{ deg}$  is found at very different velocities and can therefore be thought of as belonging to the main Sextans population. This group of 9 stars do not only share very similar distances and kinematics but also metallicities, with an average metallicity of  $[\text{Fe}/\text{H}] = -2.6$  and a scatter of 0.15 dex. Note that the average metallicity error for the stars in the substructure is 0.29 dex, much larger than the measured scatter in the metallicity, which means that the intrinsic scatter is going to be much lower than 0.15 dex. The similar metallicity of the stars found in the cold kinematic substructure would point to these stars previously belonging to a single stellar population, i.e. a stellar cluster.

Note that the information on metallicity is useful for such kind of detections: when considering all the stars together in the inner bin, with no distinction made on metallicity, the velocity dispersion is much larger, consistent with the rest of the galaxy.

Assuming that the ratio of stars in the substructure (9) with respect to the total number of probable Sextans members (174) is representative, then the substructure would account for 5% of the overall Sextans population. Assuming a luminosity for Sextans from Table 1 and a stellar mass-to-light ratio  $(M/L)_{\text{lum},V} = 2$  typical of globular clusters (Illingworth 1976; Pryor et al. 1988) as plausible for an old stellar population, then crude estimates of the total luminosity and mass of this structure are  $2.2 \times 10^4 L_{\odot}$  and  $4.4 \times 10^4 M_{\odot}$ . If this substructure is the same one found in Kleyna et al. (2004), our estimated luminosity is approximately one order of magnitude smaller than what Kleyna et al. (2004) estimated, that is  $1.3 \times 10^5 L_{\odot}$ . However the estimate was carried out in a different way, where Kleyna et al. (2004) assumed that all the light in the central 10 arcmin is due to cluster debris.

We can instead assume that the estimated light in the central 10 arcmin,  $1.3 \times 10^5 L_{\odot}$ , is actually given by the sum of the light from the substructure plus the light from the overall Sextans population. We then use the value of the central surface brightness from Irwin & Hatzidimitriou

<sup>4</sup> Here with  $\sigma$  we denote the error in the determined average velocity for the substructure.



(1995) - derived excluding the central point giving raise to the sharp central rise in the light distribution of Sextans - to estimate the contribution of the overall Sextans population to the light in the central 10 arcmin: this is about  $7.8 \times 10^4 L_\odot$ . Therefore the contribution of the substructure would then amount to  $5.2 \times 10^4 L_\odot$ , much closer to our estimate. It is therefore possible that the substructure here detected is the same one as in the work of Kleyna et al. (2004).

The properties we find are compatible with other cold substructures found in other dSphs, such as in Ursa Minor by Kleyna et al. (2003), in Sculptor (Battaglia 2007) and at projected distances of about 1 core radius in Sextans (Walker et al. 2006). This luminosity corresponds to an absolute  $M_V = -6.2$ , which is similar to globular clusters found in the Fnx, Sagittarius dSphs and in other dwarf galaxies (e.g., see van den Bergh 2006).

To date, the most metal-poor known globular cluster resides in the Fnx dSph, with high resolution measurements yielding a  $[\text{Fe}/\text{H}] = -2.5$  (Letarte et al. 2006). If the stars in the cold substructure here detected do indeed belong to the remnant of a disrupted globular cluster, the  $[\text{Fe}/\text{H}]$  values we measure would place it among the most metal poor globular clusters known. Given the large error-bars of the individual CaT measurements for these stars, determinations from high resolution spectroscopic measurements would be needed to place this on a secure foot. Detection of the O-Na anti-correlation would confirm the hypothesis.

Note that the CaT  $[\text{Fe}/\text{H}]$  values are calculated assuming that the stars in the substructure are at the same distance of Sextans. If those stars are actually an external feature, then the  $[\text{Fe}/\text{H}]$  values would not be correct. However, given the average velocity of the substructure well within  $1\sigma_{\text{GSR}}$  from the systemic velocity of Sextans, it is likely that these stars do indeed belong to the dSph.

## 5 MASS DETERMINATION

We determine the mass of Sextans by means of Jeans modeling of a spherical and stationary system assuming different dark matter density profiles.

The methodology we use consists of comparing the observed l.o.s. velocity dispersion  $\sigma_{\text{los}}$  for each distance bin with that predicted from the Jeans modeling for different models of the dark matter density profile and hypothesis on the velocity anisotropy of the tracer<sup>5</sup> (see Sect. 5.1). We explore the space of parameters which define each model and determine the  $\chi^2$  as:

$$\chi^2 = \sum_{i=1}^{N_{\text{bins}}} \left( \frac{\sigma_{\text{los}_i} - \sigma_{\text{los}}(R_i; p_\beta, p)}{\epsilon_i} \right)^2. \quad (2)$$

The variable  $p$  denotes a characteristic mass parameter of each dark matter model,  $p_\beta$  denotes a parameter describing the behaviour of the velocity anisotropy (see Sect. 5.2). Finally,  $\epsilon_i$  is the error in the observed l.o.s. velocity dispersion. The best-fitting parameters are defined as those for

which  $\chi^2$  is minimized. We quote as errors in the individual parameters the projections of the  $\Delta\chi^2 = 2.3$  region (corresponding to the region of 68.3% joint probability for a two free parameters  $\chi^2$  distribution).

### 5.1 Predicted velocity dispersion profile

The Jeans equation for a stationary spherical system in absence of net streaming motions in any of the directions is (Binney & Tremaine 1987):

$$\frac{1}{\rho_*} \frac{d(\rho_* \sigma_{r,*}^2)}{dr} + \frac{2\beta \sigma_{r,*}^2}{r} = -\frac{d\phi}{dr} = -\frac{V_c^2}{r} \quad (3)$$

where  $\rho_*$  is the density of the tracer;  $\beta$  is the velocity anisotropy parameter, defined as  $\beta = 1 - \sigma_{\theta,*}^2/\sigma_{r,*}^2$ , assuming  $\sigma_{\theta,*}^2 = \sigma_{\phi,*}^2$ ;  $\sigma_{r,*}$ ,  $\sigma_{\theta,*}$  and  $\sigma_{\phi,*}$  are the velocity dispersions in the  $(r, \theta, \phi)$  direction respectively;  $\phi$  and  $V_c$  are the potential and the circular velocity of the total mass distribution. Note that  $\beta = 0$  if the velocity ellipsoid is isotropic,  $\beta = 1$  if the ellipsoid is completely aligned with the radial direction, and  $\beta < 0$  for tangentially anisotropic ellipsoids.

The quantity to compare to the observations is the l.o.s. velocity dispersion of the tracer population (Binney & Mamon 1982):

$$\sigma_{\text{los}}^2(R) = \frac{2}{\Sigma_*(R)} \int_R^\infty \frac{\rho_*(r) \sigma_{r,*}^2}{\sqrt{r^2 - R^2}} r (1 - \beta \frac{R^2}{r^2}) dr \quad (4)$$

where  $R$  is the projected radius (on the sky) and  $\Sigma_*(R)$  is the mass surface density of the tracer.

We refer to Mamon & Lokas (2005) for the derivation of the l.o.s. velocity dispersion profile from the Jeans equation using different hypotheses on  $\beta$ .

As the discovery of multiple stellar populations in dSphs is a recent one, traditionally dSph galaxies have been treated as single component systems. In Battaglia et al. (2008) we modelled each stellar component separately in the Sculptor dSph, showing that this allows to relieve some of the degeneracies. This kind of analysis needs imaging such that the surface number density profiles of the different components can be accurately determined. This is not the case to date for Sextans, therefore until better photometric data will come we will treat all the stars in Sextans as in one component.

Below we discuss in detail the ingredients to solve the Jeans equation.

- **The spatial distribution of the tracer:** Irwin & Hatzidimitriou (1995) found that the surface brightness profile of Sextans is best fit by an exponential profile with scale radius  $R_e = 15.5'$ . This is equivalent to assuming a Sersic profile with Sersic radius  $R_S = 15.5'$  and shape parameters  $m = 1$  as done by Walker et al. (2007) and Lokas (2009). For the mass-to-light ratio we use  $(M/L)_V = 1$   $(M/L)_{V,\odot}$  and luminosity and distance from Table 1.

The 3D density profile is derived from the surface brightness profile through inversion of Abel integrals, assuming that the stars are spherically distributed. We refer to Lokas et al. (2005) for all the relevant formulas.

- **The kinematics of the tracer - Velocity gradient:** The expression for the projected velocity dispersion (Eq. 4), which measures the projected random motion in a galaxy, has been derived for the hypothesis that the system is not rotating. In systems where the rotation law can be accurately derived and there is enough statistics to derive the

<sup>5</sup> By “tracer population” we mean those objects whose kinematics can be used to recover properties of the total potential. In this case our tracers are the spectroscopically observed red giant branch stars.

dispersion profile along both the major and minor axes, one can use the Jeans equations in cylindrical coordinates. The present coverage of this dataset does not allow this alternative. Therefore we use the observed l.o.s. velocity dispersion profile derived from the rotation subtracted individual velocities.

• **The kinematics of the tracer - Velocity anisotropy:** Since the variation of the velocity anisotropy with radius is not known (as this requires proper motions), we consider two hypotheses:  $\beta$  constant with radius; and using the Osipkov-Merritt parametrization for  $\beta$  (Osipkov 1979; Merritt 1985)

$$\beta_{\text{OM}} = r^2 / (r^2 + r_a^2) \quad (5)$$

where  $r_a$  is the anisotropy radius. In the Osipkov-Merritt parametrization the anisotropy is always  $\geq 0$ , i.e. it is never tangential. The central regions are isotropic, and for  $r_a \rightarrow \infty$  the anisotropy becomes purely radial. At  $r = r_a$ ,  $\beta = 0.5$ . The smaller  $r_a$ , the faster the anisotropy becomes very radial. Models with large  $r_a$  correspond to models with almost isotropic behaviour.

• **Total mass distribution:** Since from previous works the contribution of the stars to the overall potential has been shown to be negligible in Sextans and in dSphs in general, we consider the dark matter halo as the only contributor to the kinematics of the tracer population.

We consider two different models for a spherically symmetric dark-matter halo potential:

- *Pseudo-Isothermal sphere.* This model has been extensively used in the context of extragalactic rotation curve work (see Swaters et al. 2000, and references therein). The density profile associated to this model is:

$$\rho(r) = \rho_0 \frac{r_c^2}{(r_c^2 + r^2)}, \quad (6)$$

where  $r_c$  is the core radius,  $\rho_0 = \frac{V_c^2(\infty)}{4\pi G r_c^2}$  is the central density and  $V_c(\infty)$  is the asymptotic circular velocity. At large radii the density behaves as  $\rho \propto r^{-2}$ .

The resulting mass profile is:

$$M(< r) = 4\pi\rho_0 r_c^2 \left( r - r_c \arctan \frac{r}{r_c} \right). \quad (7)$$

The profile is completely defined by  $\rho_0$  and  $r_c$ , or any couple of non-degenerate parameters.

- *NFW model.* This profile is motivated by cosmological N-body simulations in a CDM framework (Navarro et al. 1996, 1997). In this case the DM density profile is given by

$$\rho(r) = \frac{\delta_c \rho_c^0}{(r/r_s)(1 + r/r_s)^2} \quad (8)$$

where  $r_s$  is a scale radius,  $\rho_c^0$  the present critical density and  $\delta_c$  a characteristic over-density. The latter is defined by  $\delta_c = \frac{100 c^3 g(c)}{3}$ , where  $c = r_v/r_s$  is the concentration parameter of the halo,  $r_v$  its virial radius, and  $g(c) = (\ln(1+c) - c/(1+c))^{-1}$ . The concentration  $c$  has been found to correlate with the halo virial mass  $M_v$  in the range  $10^{11} - 10^{14} h^{-1} M_\odot$  (Navarro et al. 1997; Bullock et al. 2001; Wechsler et al. 2002), so that at a given redshift more massive haloes have lower concentrations. In principle, the relation between  $c$  and  $M_v$  makes the NFW model completely defined by one parameter (e.g.,  $M_v$ ). However at a fixed

mass the scatter in the predicted concentration is large, of the order of  $\Delta(\log_{10} c) = 0.18$  (Bullock et al. 2001), thus we do not consider the NFW density profile as a one-parameter family, but we describe it both by the concentration  $c$  and by the virial mass or the circular velocity at the virial radius.

At large radii (for  $r \gg r_s$ ), the density behaves as  $\rho \propto r^{-3}$ , and therefore, the total mass diverges logarithmically. The resulting mass profile is

$$M(< r) = M_v \frac{f(x)}{f(c)} \quad (9)$$

where  $x = r/r_s$  and  $f(x) = \ln(1+x) - \frac{x}{1+x}$  (Klypin et al. 2002).

When integrating Eq. 4, we set the upper integration limit to  $r_v$  where we use  $r^{2\beta} \rho_* \sigma_{r,*}^2|_{r_v} = 0$  (we are essentially assuming that the particles are bound out to the virial radius). As we will see in the next Section and as it is found in previous works on dSphs, the extent of the luminous matter is typically one order of magnitude smaller than the extent of the best-fitting DM halo, thus setting the upper integration limit to  $r_v$  instead of to infinity will not affect our results, only decrease the computation time.

## 5.2 Results

We perform the fitting procedure for the observed l.o.s. profile derived in Sect. 4.3.1, i.e. “Binning2”<sup>6</sup>. The parameter  $p$  in Eq. 2 denotes the mass enclosed within the last measured point for the isothermal sphere and the virial mass for the NFW model; the parameter  $p_\beta$  is  $p_\beta = \beta$  for the models using  $\beta$  constant with radius and  $p_\beta = r_a$  for the models using  $\beta_{\text{OM}}$ .

The results are summarized in Tab. 3.

• **Isothermal sphere:** In this model the total mass of the DM halo is not finite, therefore we choose to fit the value of the mass within the last measured point,  $M(< R_{\text{last}})$ , which for “Binning2” is  $R_{\text{last}} = 2.36$  kpc. The other free parameter to take into account is the velocity anisotropy  $\beta$ .

We explore the performance of models with core radii  $r_c = 0.001, 0.05, 0.1, 0.5, 1, 1.5, 2, 2.5$  and 3 kpc. In practise, we fix the core radius to each of these values and minimize the  $\chi^2$  to obtain the best-fitting  $M(< R_{\text{last}})$  and  $\beta$ . The results of the fits are summarized in the plots shown in Fig. 14 (left). At a given core radius, the best fit models with constant  $\beta$  give in general smaller  $\chi^2$  values than when  $\beta = \beta_{\text{OM}}$ . The models for  $\beta = \beta_{\text{OM}}$  and  $r_c < 0.5$  kpc have a reduced  $\chi^2 > 3$ , which for 4 degrees of freedom corresponds to a significance level of less than 2%; they can therefore be considered as statistically unacceptable. All the other best fitting models for the explored core radii have reduced  $\chi^2 \lesssim 1$ , therefore they are all statistically acceptable. For these models the best-fitting  $M(< R_{\text{last}})$  ranges from  $\sim 1 - 4 \times 10^8 M_\odot$  (smaller core radii, smaller masses); the best-fitting anisotropies ranges from  $-6$  to  $0.5$  for  $\beta = \text{const}$

<sup>6</sup> We checked that using the “Binning3” velocity dispersion profiles produces best-fitting parameters and models that are very similar to those obtained when adopting the “Binning2” profile, although in this case the minimum  $\chi^2$  values for the best-fitting models are larger than the ones from “Binning2”.

(smaller core radii more tangential anisotropies), while the anisotropy radius goes from 2 to 15 kpc (the upper limit of the explored  $r_a$ ), forcing the anisotropy to be close to zero. The models with the smallest reduced  $\chi^2$  (see Fig.15) for  $\beta = \text{const}$  have  $r_c = 3$  kpc ( $M(< R_{\text{last}}) = 4 \pm 0.8 \times 10^8 M_\odot$  and  $0.06 < \beta < 0.6$ ) and for  $\beta = \beta_{\text{OM}}$   $r_c = 1.5$  kpc ( $M(< R_{\text{last}}) = 3.2 \pm 0.7 \times 10^8 M_\odot$  and  $r_a > 1.5$  kpc).

This tendency for increasing tangential anisotropy with decreasing core radius comes from the fact that smaller core radii models have higher concentrations of mass in the central regions and this tends to increase the central value of the velocity dispersion. To match a nearly constant velocity dispersion profile the anisotropy then needs to be tangential.

• **NFW model:** For this model we let the concentration vary from  $c=10, 15, 20, 25, 30, 35$ , and for each of these values we derive the best-fitting virial mass and velocity anisotropy. Using an extrapolation of the formulae in the N-body simulations of Jing (2000) (see Koch et al. 2007), the concentrations adopted here would correspond to the concentrations expected for haloes with virial masses in the range  $10^6$ - $10^{12} M_\odot$  (smaller mass larger  $c$ ) well containing the range of virial masses expected for dSphs.

At fixed concentration, all the models with  $\beta = \beta_{\text{OM}}$  have reduced  $\chi^2$  larger than then models with  $\beta = \text{const}$ . The models with  $c \geq 20$  have a reduced  $\chi^2 > 2.5$ , corresponding to a significance level of less than 5% for 4 degrees of freedom and have therefore low statistical significance. The best result for the  $\beta = \text{const}$  case is also given by the model with  $c = 10$ , with a virial mass  $M_v = 2.6 \pm 0.8 \times 10^9 M_\odot$  and  $\beta = -0.6_{-1.4}^{+0.6}$  (see Fig.15). All the models with  $\beta = \text{const}$  have reduced  $\chi^2$  between 1 and 1.5, where the virial masses range from approximately  $3 \times 10^8$  to  $2.6 \times 10^9 M_\odot$  (smaller  $c$  larger virial mass), which gives a mass within the last measured point of  $1.2 \times 10^8 M_\odot$ , and  $\beta$  goes from about  $-4.5$  to  $-0.6$  (smaller  $c$  less tangential  $\beta$ ). This also explains why most of the models with  $\beta = \beta_{\text{OM}}$  are not favoured for NFW profiles: in the hypothesis of  $\beta = \text{const}$ , which yields a good fit to the data, the best-fitting anisotropies are mildly tangential; since in the  $\beta = \beta_{\text{OM}}$  the anisotropy is forced to be positive, than the resulting model cannot reproduce the data as well.

We conclude that because of the well-known mass-anisotropy degeneracy, it is not possible to firmly distinguish between a cored and a cuspy dark matter distribution, nor about different hypothesis of anisotropy, solely on the basis of the line-of-sight velocity dispersion profile. The only models that can be excluded among the explored ones because of their large  $\chi^2$  values are the NFW models with  $\beta = \beta_{\text{OM}}$  and  $c \geq 20$ . However, the general trend is for the best-fitting models to have  $\beta$  close to isotropic, be it slightly tangential as for the NFW case or slightly radial as for the cored profile. Also, the tendency for cuspy profiles of low concentrations to produce better fits than for larger concentrations seems to suggest that shallower profiles are preferred. Independently on the model, we find that the mass within the last measured point of Sextans, at 2.3 kpc, should be in the range  $2.4 \times 10^8 M_\odot$ . This would give a dynamical mass-to-light ratio between 460 and 920 ( $M/L$ ) $_{V,\odot}$ .

The presence of the central substructure does not affect the mass estimate derived. Although the velocity dispersion for stars at the distance covered by the substructure,  $7.6 \pm 1.1$

km s $^{-1}$ , is lower than if these stars had not been included, i.e.  $8.6 \pm 1.4$  km s $^{-1}$ , these two values are consistent within the errors.

## 6 DISCUSSION

• **Metallicity properties:** The stars in Sextans show a wide [Fe/H] range, with the majority having [Fe/H] values between  $-3.2$  and  $-1.4$ , with an average [Fe/H] =  $-1.9$ . Among the sample of probable members, 11 extremely metal poor stars are found, reaching down to [Fe/H] =  $-3.8$ . If the stars in Sextans were formed from a pre-enriched medium, then the presence of stars with [Fe/H] as low as  $-3.8$  suggests that this interstellar medium most likely had not been pre-enriched to a larger value.

Sextans exhibits a clear spatial variation of its metallicity properties: the region at projected radius  $R < 0.8$  deg displays the whole range of metallicities, while at larger projected radii practically only stars more metal poor than [Fe/H]  $\sim -2.2$  are present. Photometric studies of its stellar population show an age difference of at least 3 Gyr between the central and outer parts of Sextans, with the central parts containing stars between 10 and 14 Gyr old and the outer parts mostly 14 Gyr old stars. It appears then that the outer parts were formed very quickly, reaching a metallicity up to [Fe/H]  $\sim -2.2$ , while the inner parts could continue their evolution for at least 3 more Gyr and enrich to [Fe/H]  $\sim -1.4$ . One can speculate that the less prolonged star formation of the outer parts may have been caused either from external processes, which removed the gas from the external region, or to internal effects, which depleted the outer parts of gas. It is although possible that gas was still present in the outer regions for some time but simply that conditions for star formation were not met.

Similar, although less pronounced, spatial variations of metallicity properties have been detected in other dSphs, such as for example in Sculptor (Tolstoy et al. 2004), Fornax (Battaglia et al. 2006) and to a minor extent in Carina (Koch et al. 2006). There are hints that Leo I may exhibit such variations (Gullieuszik et al. 2009) although the current data are not sufficient to put this result on a firm ground. Using Strömgren photometry Faria et al. (2007) show the presence of a possible spatial variation in the metallicity properties of the Draco dSph. It is still unclear what is the driving process behind these metallicity variations. To disentangle environmental effects from internal evolution it is important to obtain observations of the stellar populations, kinematics and metallicity variations of isolated dwarf galaxies, outside the halo of large spirals.

• **Velocity gradient:** A statistically significant velocity gradient is found along the projected major axis and an axis at P.A. =  $191^\circ$  in our sample of 174 probable members of Sextans. Walker et al. (2008) also detect a velocity gradient in Sextans, although with lower amplitude and approximately along the minor axis of the galaxy. Pinning down the amplitude and direction of such gradients, expected to be small for dSphs, would require large sample of stars not only in the central regions of the object but also in the outer parts, so that the trends along various directions may be accurately determined. Unfortunately this is very challenging

for a system like Sextans, because of its large extent on the sky and the outer parts being sparsely populated.

Also a univocal interpretation of this feature does not appear possible at this stage. One possibility is that the gradient may have originated as the result of tidal disruption of Sextans from the Milky Way, as predicted in N-body models of disrupted satellites (e.g. Oh et al. 1995). However no clear signs of tidal disruption such as tidal tails or S-shaped contours are found in Sextans that could confirm this hypothesis, although this may be just due to the observational difficulties in detecting such features (e.g. Muñoz et al. 2008), especially in a diffuse and heavily contaminated object like Sextans. Knowledge of the accurate proper motion of the galaxy would allow to reconstruct its orbital history and determine if strong interactions with the Milky Way may have occurred. However no direct determinations of the proper motion of Sextans are available yet in the literature. Such determinations would also allow to understand whether the observed gradient may merely be a geometrical effect due to the projection of the object transverse motion along the line-of-sight because of its large extent on the sky, since in this case the direction of the maximum gradient is expected to be aligned with the proper motion direction.

Another possible option is that the velocity gradient is due to intrinsic rotation of the object. In this case, if the flattening of Sextans is due to intrinsic rotation, then it would be reasonable to expect the maximum gradient along the projected major axis of the object, as detected in our data. When rotation is responsible for the flattening of an axisymmetric galaxy, a simple relation holds between the true ellipticity of the galaxy and its mass weighted rotational velocity over the mass weighted velocity dispersion,  $v_0/\sigma_0$  (Binney & Tremaine 1987). As for estimate of the rotational velocity we use the fitted value of the gradient at  $R \sim 0.7$  deg, the distance of the outermost stars along the major axis which cause the rotation signal in our data-set: this value is  $v_{\text{rot,los}} = 5.9 \text{ km s}^{-1}$  and it is likely to represent a lower limit to the maximum rotational velocity. Replacing  $\sigma_0$  by the velocity dispersion measured along the line-of-sight, and  $v_0$  by  $v_{\text{rot,los}}$ , the ratio  $v_{\text{rot,los}}/\sigma_{\text{GSR}} = 0.7$  is very close to the value expected for an “isotropic rotator” (0.727) of ellipticity  $e = 0.35$  (Binney & Merrifield 1998, as tabulated in the). This means that the shape of Sextans is consistent with being flattened by rotation, although due to the fact that Sextans velocity ellipsoid and inclination are unknown, it is possible that velocity anisotropy is also contributing to the flattening of the galaxy.

At the moment it is still difficult to build a coherent picture not only on the cause of velocity gradients in Milky Way dSphs, but of even their presence. No significant gradient is found in Leo II (Koch et al. 2007) where the coverage is very homogeneous. Battaglia et al. (2008) found a significant velocity gradient along the projected major axis of the Sculptor dSph, confirmed by Walker et al. (2009). Gradients of smaller amplitudes have also been detected in Carina and in Fornax (Walker et al. 2009), in this case along directions close to the projected minor axis of the object. For those two objects the amplitude and direction of the gradient are consistent with being due to the transverse motion of the object along the line-of-sight, given their measured proper motion. However, while Carina has a very homogeneous coverage, this is not the case for Fornax, where the outer parts still

await careful scrutiny. The outer parts of these objects appear to be particularly important in the measurement of velocity gradients, as shown by the case of Leo I: Mateo et al. (2008) found a highly statistically significant gradient when considering only the stars located at projected distances larger than  $400''$ , while they found no significant gradient neither when using the sample of stars at smaller projected distances, nor when considering the whole sample (which is dominated in number by the stars at  $R < 400''$ ). Also combining data-sets together may give different results: when using only their GMOS dataset Koch et al. (2007) find no statistically significant gradient in Leo I, while when combining their GMOS dataset to their DEIMOS one the statistical significance of the detected gradient increases.

This wealth of results on the different Milky Way dSphs shows that a coherent picture of velocity gradients as intrinsic feature in dSphs is still lacking, and so probably are datasets with both large enough statistics and homogeneous coverage to pin down values and directions of these gradients.

Velocity gradients have been detected along the projected major axis of the 2 isolated dSphs of the Local Group: Cetus and Tucana (Lewis et al. 2007; Fraternali et al. 2009, respectively)<sup>7</sup>. At the distance of Cetus and Tucana, unless of invoking three-body interactions or such (Sales et al. 2007), tidal stripping from either the Milky Way or M31 cannot have been important, therefore it is very unlikely that the detected gradients may be attributed to tides. Also, gradients due to the transverse motion of the system are expected to be negligible due to the small extent on the sky of these objects. This would point to velocity gradients as being an intrinsic feature of these systems.

Also other spheroidal systems in the Local Group do show velocity gradients along their projected major axis. Geha et al. (2010) found significant rotation in the NGC 147 and NGC 185 dEs. The authors calculate that the flattening of these galaxies is consistent with the amount of rotation found, although part of it may be due to anisotropy. These galaxies are dEs, not dSphs, with luminosities of the order of  $10^8 L_\odot$ , about 2 orders of magnitude larger than the common dSph, and 1 order of magnitude larger than Fornax. However, as discussed in Kormendy et al. (2009) and Tolstoy et al. (2009), the dEs in the Local Group (NGC 147, NGC 185 and NGC 205) share similarities with the dSphs, suggesting that these may be the high luminosity end of the sequence.

• **Mass determination:** We have performed a Jeans analysis of the observed line-of-sight velocity dispersion profile of Sextans and find that for the best fitting cored profiles the mass within the last measured point ranges from  $3.2\text{--}4 \times 10^8 M_\odot$ , while the mass within the last measured point for the best fitting NFW profile is smaller,  $1.9 \pm 0.6 \times 10^8 M_\odot$  but consistent within  $1\sigma$  with the determination from the cored profiles. This mass range implies that Sextans contains between about 450-900 times more dark than luminous matter, in the typical range of Milky Way dSphs.

Other authors have estimated the mass of Sextans at smaller distances from the centre. The mass that

<sup>7</sup> Note though that in these two cases directions other than the major axis have not been well explored.

Walker et al. (2007) find within their last measured point at 1.1 kpc is  $5.4 \times 10^7 M_\odot$  for a constant anisotropy and an NFW halo (with best-fitting  $M_v = 3 \times 10^8 M_\odot$  and  $c = 20$  derived from the concentration-virial mass relation in Jing 2000 and best-fitting  $\beta = -2$ ). This is consistent with our model with  $c = 20$ , which yields  $M_v = 6_{-1.5}^{+2.5} \times 10^8 M_\odot$  and  $\beta = -1.7$  and  $M(<1.1 \text{ kpc}) = 5.5_{-1.4}^{+2.3} \times 10^7 M_\odot$ . Note that in their analysis Walker et al. (2007) choose to fix the concentration to the virial mass according to the formula of Jing (2000) instead of exploring various concentrations for a given virial mass like in this work. It is possible that also Walker et al. (2007) data would have yielded a lower best-fitting concentration, if the correlation  $M_v$ - $c$  was not assumed.

It has been recently shown that the determination of the dark matter mass within a certain distance is robust to model assumptions (e.g. Strigari et al. 2007). An interesting result has been that the mass enclosed within 0.3 (0.6 kpc) spans a narrow range of values (Gilmore et al. 2007; Strigari et al. 2007, 2008) and this could imply a minimum mass scale for the existence of luminous satellites (see also Mateo 1998, for a similar suggestion). In the determination of Strigari et al. (2007) the mass enclosed within 0.6 kpc for Sextans is  $M(<0.6 \text{ kpc}) = 0.9_{-0.3}^{+0.4} \times 10^7 M_\odot$  for a dark matter halo consistent with CDM predictions. For comparison, our best-fitting NFW model gives  $M(<0.6 \text{ kpc}) = 2.0 \pm 0.6 \times 10^7 M_\odot$ , consistent within  $2\sigma$ . Our best-fitting cored profiles instead give  $M(<0.6 \text{ kpc}) = 0.9 \pm 0.2 \times 10^7 M_\odot$  (constant  $\beta$ ) and  $M(<0.6 \text{ kpc}) = 1.0 \pm 0.2 \times 10^7 M_\odot$ , both very similar to the estimate of Strigari et al. (2007). Therefore in this case Sextans would fit in the picture of a minimum mass scale for dSphs. Note that the mass within such a small distance from the centre, while it appears to come out naturally from CDM models, is not very informative on the total dark matter content of the satellite: while the enclosed mass within 0.6 kpc spans 1 order of magnitude ( $\sim 10^7$  and  $\sim 10^8 M_\odot$ ), the total dark matter mass may span about 3 orders of magnitude, as a consequence of the lack of a tight correlation between concentration and virial mass, and of the particular (accretion and orbital) history of the satellite (Li et al. 2009).

Walker et al. (2009, 2010) have expanded the above results to the mass enclosed within the half-light radius and also propose that all dSphs may be embedded in a dark matter halo of similar mass (and mass profile). The mass within the half-light radius (estimate from Walker et al. 2010, adjusted for the distance to Sextans here assumed) that we derive for the best-fitting NFW model ( $c = 10$ ) is  $M(<0.7 \text{ kpc}) = 2.6 \pm 0.8 \times 10^7 M_\odot$ , in remarkable agreement with the determination of Walker et al. (2010)<sup>8</sup>. The best-fitting cored dark matter models however give lower values,  $1.4 \pm 0.2 \times 10^7 M_\odot$  ( $r_c = 3 \text{ kpc}$  and  $\beta = \text{const}$ ) and  $1.7 \pm 0.4 \times 10^7 M_\odot$  ( $r_c = 1.5 \text{ kpc}$  and  $\beta = \beta_{\text{OM}}$ ). These estimates make Sextans fall below the “universal” mass relation for dSph galaxies in Walker et al. (2010). Until degeneracies between different dark matter models are relieved, it is pos-

sible that universal relations between dSphs mass and other properties may change according to the adopted models.

Finally, we would like to point out that for small galactic systems such as dSphs the total mass is likely to be an important factor in determining their evolution. Indeed the depth of the potential well will influence how much of the gas and metals can be retained and therefore the subsequent star formation and chemical enrichment history from the system and how much will be expelled because of for example supernovae explosions (e.g. Revaz et al. 2009). Since outside the last measured point one can only extrapolate mass values, it will not be possible to determine total dSph masses with the current methods. However, determination as far out as possible are still important so as to provide constraints for models that aim at reproducing the detailed observed properties of stars in dSphs.

## 7 SUMMARY

We obtained VLT/FLAMES intermediate resolution ( $R \sim 6500$ ) spectroscopic observations in the NIR CaT region for 1036 distinct targets along the line-of-sight to Sextans, with magnitudes and colours broadly consistent with RGB stars. This resulted into 789 stars with S/N and error in velocity such as to produce reliable line-of-sight velocities and CaT EWs. Among those, 174 are RGB stars probable members of Sextans with line-of-sight velocities accurate to  $\pm 2 \text{ km s}^{-1}$  and CaT [Fe/H] measurements accurate to  $\pm 0.2 \text{ dex}$ .

The vast majority of the Galactic contaminants could be weeded out from the sample using a simple  $3\sigma$  kinematic cut. We refined our membership criteria by using the Mg I line at  $8806.8 \text{ \AA}$  as an empirical indicator of stellar surface stellar gravity, and therefore distinguish between probable members of the dSph (RGB stars) and Galactic contaminants (most likely dwarf stars).

We used the sample of probable members to investigate the wide-field metallicity and kinematic properties of Sextans, and to perform a determination of its mass content.

Sextans is a metal poor system, with an average  $[\text{Fe}/\text{H}] = -1.9$ . Its stars display a wide range of metallicities, with the majority being between  $-3.2 < [\text{Fe}/\text{H}] < -1.4$ . A spatial variation of the metallicity properties is present, with the central parts being in average more metal rich than the outer parts. There are indications of a link with the kinematics, with the stars more metal rich than  $[\text{Fe}/\text{H}] = -2.2$  having a lower dispersion than the stars with  $[\text{Fe}/\text{H}] < -2.4$ .

The analysis of the radial trend of the average velocity and dispersion of Sextans stars as function of metallicity has uncovered the presence of a cold, metal-poor ( $[\text{Fe}/\text{H}] \sim -2.6$  from CaT measurements) kinematic substructure at projected radii  $R < 0.22 \text{ deg}$ . This structure is consistent with being a disrupted stellar cluster. It is possible this may be the same feature observed by Kleyna et al. (2004).

Our sample of Sextans stars shows a statistically significant velocity gradient along the projected major axis of the galaxy and along an axis at P.A. =  $191^\circ$  ( $8.5 \pm 3.0 \text{ km s}^{-1} \text{ deg}^{-1}$  and  $7.5_{-3.0}^{+3.4} \text{ km s}^{-1} \text{ deg}^{-1}$ , respectively). Given the current global observational understanding of this object it is unclear whether this gradient is due to intrinsic rotation, tidal disruption or geometrical effects. Also, a

<sup>8</sup> Also our other NFW models though give a very similar enclosed mass ( $M(<0.7 \text{ kpc}) = 3.0 \times 10^7 M_\odot$  for  $c = 20$  and  $M(<0.7 \text{ kpc}) = 3.2 \times 10^7 M_\odot$  for  $c = 35$ ), consequence of the degeneracy between concentration and virial mass.

better sampling of the outer parts, both in terms of spatial coverage and number statistics, would allow to place the amplitude of the velocity gradient on more secure footing and perhaps determine the overall velocity pattern throughout the face of the galaxy.

In the hypothesis of dynamical equilibrium, we performed a mass determination of Sextans, following a Jeans analysis and comparing the observed line-of-sight velocity dispersion profile to the predictions for cored and cuspy dark matter models. Sextans appears to be a very dark matter dominated object, with a mass within 2.3 kpc of  $2 - 4 \times 10^8 M_\odot$ , giving a dynamical mass-to-light ratio between 460-920  $(M/L)_{V,\odot}$ . Within the explored dark matter models and velocity anisotropy profiles, the best fits are given by cored profiles with large core radius and mildly radial anisotropy. However also a NFW profile with mildly tangential anisotropy gives a very good representation of the data; the concentration of the favoured NFW is  $c = 10$  somewhat lower for what expected for galaxies in the mass range of Sextans when using the virial mass - concentration relation of Jing (2000).

## ACKNOWLEDGEMENTS

G.B. and P.P. are grateful to the Kapteyn Astronomical Institute for hospitality and financial support during part of this work. G.B. thanks F.Fraternali for useful suggestions. The authors acknowledge E.Starkenburg for kindly running preliminary models regarding the Mg I line. Financial support by the European Research Council has been provided to A.H. in the form of SZG-GALACTICA, #240271.

Parameter	value	reference
$(\alpha_{J2000}, \delta_{J2000})$	$10^h 13^m 03^s -01^\circ 36' 54''$	1
P.A.	$56^\circ$	2
$e$	0.35	2
$R_{\text{core}}$	16.6 arcmin	2
$R_{\text{tidal}}$	160 arcmin	2
$R_e$	15.5 arcmin	2
$v_{\text{sys}}$	$226.0 \pm 0.6 \text{ km s}^{-1}$	3
$v_{\text{sys, GSR}}$	$78.4 \pm 0.6 \text{ km s}^{-1}$	3
$\sigma$	$8.4 \pm 0.4 \text{ km s}^{-1}$	3
$\sigma_{\text{GSR}}$	$8.4 \pm 0.4 \text{ km s}^{-1}$	3
$(m-M)_0$	19.67	1
Distance	86 kpc	1
$L_V$	$4.37 \pm 1.69 \times 10^5 L_\odot$	2, 4
$V_{\text{HB}}$	20.35	2
$E(B-V)$	0.0477	5

**Table 1.** The various rows are from top to bottom: coordinates of the optical centre; position angle, defined as the angle between the north direction and the major axis of the galaxy measured counter-clockwise; ellipticity, defined as  $e = 1 - b/a$ ; King core and tidal radius; exponential radius; systemic velocity in the heliocentric and in the GSR system; global velocity dispersion, in the heliocentric and in the GSR system; distance modulus and heliocentric distance; luminosity in V-band (based on the apparent magnitude measured by Irwin & Hatzidimitriou 1995 but readjusted for a distance of 86 kpc by Lokas 2009); V magnitude of the horizontal branch; reddening. References: 1 = Mateo (1998); 2 = Irwin & Hatzidimitriou (1995); 3 = this work; 4 = Lokas (2009); 5 = Schlegel et al. (1998), <http://irsa.ipac.caltech.edu/cgi-bin/bgServices/nph-bgExec>, average value over 5 degrees.

Field name	RA(J2000)	DEC(J2000)	Date	Exp. time [sec]	S/N	$N_{\text{targ}}$
Sext_100	$10^h 12^m 58.1^s$	$-01^\circ 38' 05.5''$	2003-12-20	2700	18.6	54
Sext_101	$10^h 14^m 47.4^s$	$-01^\circ 11' 27.5''$	2003-12-22	3800	17.2	55
Sext_102	$10^h 13^m 22.1^s$	$-01^\circ 21' 53.6''$	2004-03-14	500, 1125, 3600	2.9, 4.5, 15.5	74, 92, 92
Sext_103	$10^h 11^m 13.3^s$	$-01^\circ 12' 01.9''$	2003-12-22	4000	13.3	50
Sext_104	$10^h 11^m 21.6^s$	$-01^\circ 31' 38.0''$	2004-03-15	3600	21.1	68
Sext_112	$10^h 13^m 38.5^s$	$-02^\circ 00' 35.6''$	2008-05-25	3600	14.0	81
Sext_113	$10^h 14^m 52.3^s$	$-02^\circ 24' 24.5''$	2004-01-01	3600	25.1	48
Sext_114	$10^h 12^m 24.1^s$	$-01^\circ 58' 43.5''$	2004-03-16	4600	17.5	83
Sext_115	$10^h 11^m 30.4^s$	$-02^\circ 09' 45.0''$	2003-12-20	3600	8.8	57
sext_ext_02	$10^h 17^m 03.1^s$	$-01^\circ 01' 49.8''$	2004-03-17	3600	26.8	76
sext_ext_03	$10^h 18^m 36.3^s$	$-00^\circ 24' 21.9''$	2004-03-18	3600	28.7	69
sext_ext_04	$10^h 20^m 43.2^s$	$-00^\circ 06' 51.4''$	2004-03-19	3600	37.4	79
sext_ext_06	$10^h 13^m 22.9^s$	$-00^\circ 26' 51.1''$	2004-03-20	4200	42.0	68
sext_ext_08	$10^h 08^m 27.4^s$	$-00^\circ 52' 01.6''$	2004-03-17	3600	31.6	58
sext_ext_14	$10^h 07^m 42.2^s$	$-03^\circ 13' 27.8''$	2004-03-20/21	2511, 3600	29.9, 33.3	66, 66
sext_ext_16	$10^h 07^m 29.2^s$	$-01^\circ 40' 19.7''$	2004-03-21	4500	27.7	57

**Table 2.** Journal of our VLT/FLAMES observations at  $R \sim 6500$  of Sextans. The columns give respectively: the name of the observed field, the coordinates of the FLAMES pointing, the UT date of observation, the exposure time, the median signal-to-noise and the number of the observed spectra. All these observations were taken in service mode by ESO staff. Field 102 and ext\_14 have repeated exposures because the first exposures did not meet the required criteria for the maximum allowed seeing and/or airmass. This repeated exposures also allow a check for the internal velocity and EWs errors.

	$\chi^2$	$\chi^2/\nu$	$p_\beta$	$M(< R_{\text{last}})$	$M_V$
Cored $r_c = 3.0 \text{ kpc } \beta = \text{const}$	0.73	0.2	$0.06 < \beta < 0.6$	$4.0 \pm 0.7 \times 10^8 M_\odot$	
Cored $r_c = 1.5 \text{ kpc } \beta = \beta_{\text{OM}}$	2.5	0.6	$r_a > 1.5 \text{ kpc}$	$3.2 \pm 0.7 \times 10^8 M_\odot$	
Cuspy $c = 10 \beta = \text{const}$	2.9	0.7	$-1.4 < \beta < 0$	$1.9 \pm 0.6 \times 10^8 M_\odot$	$2.6 \pm 0.8 \times 10^9 M_\odot$

**Table 3.** Parameters of the best-fitting dark matter models for mass modelling of Sextans, when using the observed l.o.s. velocity dispersion profile from “Binning2”. The columns show: the  $\chi^2$ , the reduced  $\chi^2$  (with the number of degrees of freedom being  $\nu = 4$ ), the parameter defining the anisotropy (i.e.  $\beta$  itself for the  $\beta = \text{const}$  case, and the anisotropy radius  $r_a$  [kpc] for the  $\beta = \beta_{\text{OM}}$  case), the mass contained within the last measured point (at  $\sim 2.3$  kpc, assuming a distance to Sextans of 86 kpc), and for the cuspy profile the virial mass.

Name	$\alpha_{J2000}$	$\delta_{J2000}$	S/N	$v_{\text{hel}}$ [km s <sup>-1</sup> ]	$\Sigma W$ [Å]	[Fe/H]
sext_000	10 12 40.27	-1 29 7.7	13.0	$241.51 \pm 4.64$	$2.28 \pm 0.46$	$-2.34^{+0.27}_{-0.31}$
sext_001	10 12 47.98	-1 29 38.8	22.7	$222.51 \pm 1.70$	$3.44 \pm 0.26$	$-1.78^{+0.13}_{-0.13}$
sext_002	10 12 39.03	-1 29 59.0	34.6	$235.84 \pm 1.22$	$3.81 \pm 0.17$	$-1.87^{+0.08}_{-0.08}$
sext_003	10 13 9.94	-1 29 34.9	21.7	$241.29 \pm 2.81$	$2.93 \pm 0.28$	$-1.95^{+0.15}_{-0.15}$
sext_004	10 13 18.97	-1 26 58.2	20.0	$216.48 \pm 2.40$	$1.96 \pm 0.30$	$-2.53^{+0.20}_{-0.23}$
sext_005	10 13 17.14	-1 26 38.1	22.9	$245.40 \pm 1.48$	$2.54 \pm 0.26$	$-2.27^{+0.14}_{-0.15}$

**Table 4.** This table lists the relevant data for the stars in Sextans observed with VLT/FLAMES which passed our membership criteria. The columns indicates: (1) the star ID; (2),(3) star coordinates (right ascension in hours and declination in degrees); (4) S/N/Å ; (5) heliocentric velocity and its error; (6) summed CaT equivalent width ( $EW_2 + EW_3$ ) and its error; (7) [Fe/H] value and error, derived adopting the calibration from Starkenburg et al. (2010).

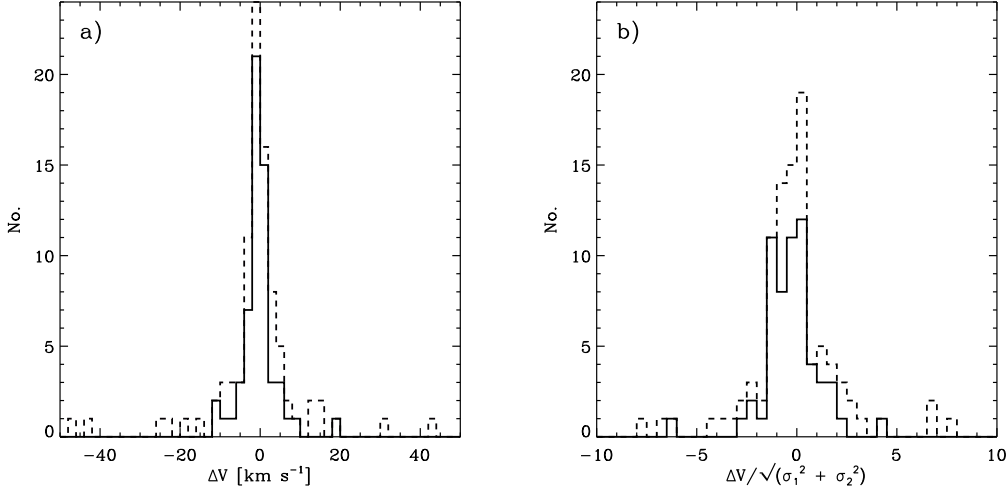


**Figure 1.** Comparison between velocity measurements for stars with double measurements in the Sextans dSph. Panel a) Distribution of velocity differences for all the stars (dashed line), and for the stars with S/N per Å  $\geq 10$  and estimated error in velocity  $\leq 5$  km s<sup>-1</sup> for each measurement (solid line). The weighted mean velocity, *rms* dispersion and scaled median absolute deviation from the median (where the scaled median absolute deviation from the median (MAD) is  $1.48 \times \text{MAD} \equiv$  a robust *rms* e.g. Hoaglin et al. 1983) are:  $0.9 \pm 3.0$  km s<sup>-1</sup>,  $29.0 \pm 2.2$  km s<sup>-1</sup>,  $4.3$  km s<sup>-1</sup> (dashed line) and  $-0.6 \pm 0.5$  km s<sup>-1</sup>,  $2.5 \pm 0.5$  km s<sup>-1</sup>,  $2.0$  km s<sup>-1</sup> (solid line). Panel b) As above but now the velocity difference is normalised by the predicted error. With these S/N and velocity error cuts the measured error in the velocity distribution is close to the expected unit variance Gaussian ( $1.48 \times \text{MAD} = 0.98$ ).



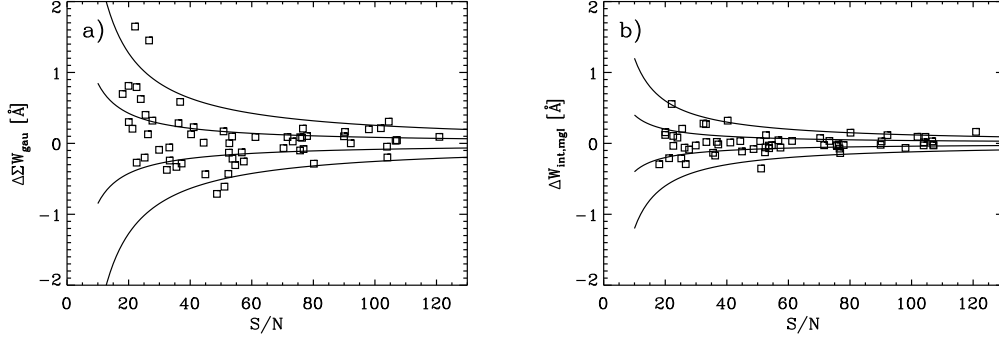


**Figure 2.** Comparison between EW measurements for stars with double measurements in the Sextans dSph. Distribution of summed CaT EW ( $EW_2 + EW_3$ ) differences from Gaussian fit (left) and MgIEW differences from integrated flux (right) as a function of S/N for the stars with S/N per Å  $\geq 10$  and estimated error in velocity  $\leq 5$  km s $^{-1}$  for each measurement. Assuming a similar S/N for the individual measurements of each star, the error in the summed CaT EW difference is  $\sqrt{2} \times \sigma_{\Sigma W} = \sqrt{2} \times 6/(S/N)$  while the error in the MgIEW difference is  $\sqrt{2} \times \sigma_{\Sigma W} = \sqrt{2} \times 2.8/(S/N)$ . The solid lines indicate the 1 and 3  $\sigma$  region for the error in the difference of summed EW. The weighted mean summed CaT EW difference, *rms* dispersion in the difference and scaled MAD are  $0.03 \pm 0.05$  Å,  $0.22 \pm 0.06$  Å, 0.25 Å. The weighted mean in the MgIEW difference, *rms* dispersion and scaled median absolute deviation from the median are  $0.01 \pm 0.02$  Å,  $0.09 \pm 0.03$  Å, 0.08 Å.

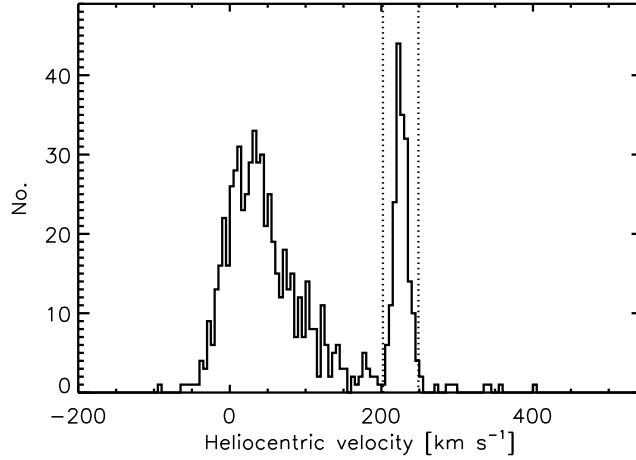


**Figure 3.** Distribution of heliocentric velocities for the stars observed with VLT/FLAMES in the direction of Sextans and that met our selection criteria. The dotted lines indicate the region used for the 3- $\sigma$  membership selection.

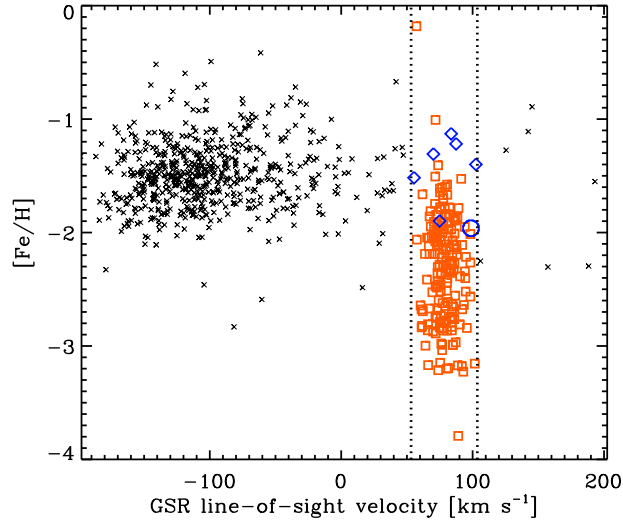


**Figure 4.**  $[\text{Fe}/\text{H}]$  versus GSR line-of-sight velocity for the observed VLT/FLAMES targets (crosses and squares show the stars outside and within the  $3\sigma$  membership region, respectively; the vertical dotted lines show the velocity membership region). Note that the stars found outside the  $3\sigma$  membership region, which are probable Galactic contaminants, tend to be preferentially found in the range  $-2.0 \lesssim [\text{Fe}/\text{H}] \lesssim -0.5$ . This means that Sextans stars at  $[\text{Fe}/\text{H}] \lesssim -2.0$  are less likely to be contaminated by Galactic stars whose velocity falls in the  $3\sigma$  membership selection region. The diamonds indicate stars with velocity consistent with membership but with Mg I EW too large for giant stars (see text). The circle indicates one object with velocity and Mg I EW consistent with membership but with unusual position on the CMD (see text).

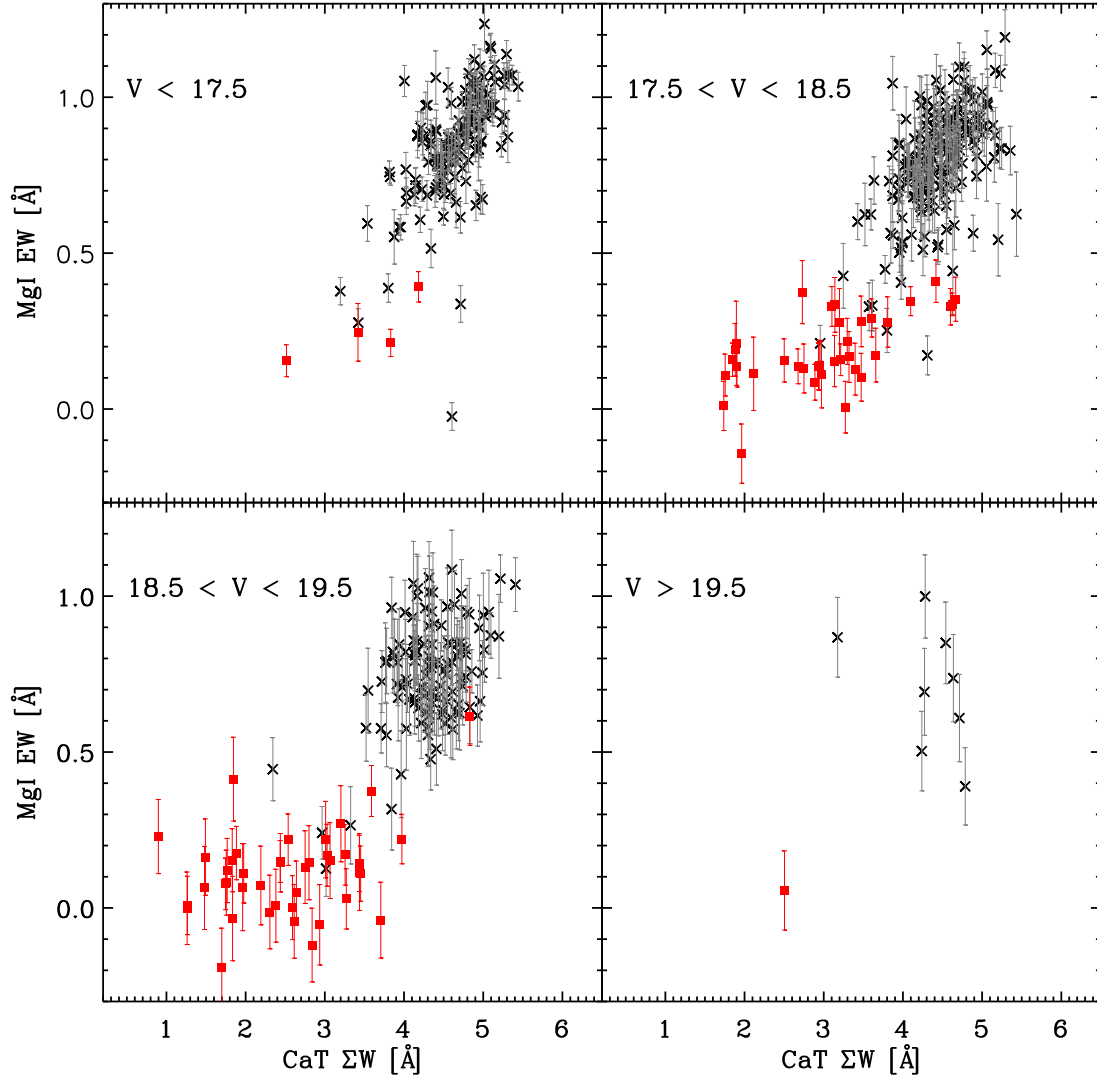


**Figure 5.** Mg I EW vs CaT  $\Sigma W$  in bins of  $V$  magnitude. The range of magnitudes are indicated on the top left corner of the panels. The filled red squares show the stars which are highly probable Sextans members (i.e. with velocities within  $\pm 2\sigma$  from the systemic velocity of Sextans) and the open black squares the stars which are highly likely to be MW contaminants (i.e. with velocities at least  $4\sigma$  away from the systemic velocity of Sextans).

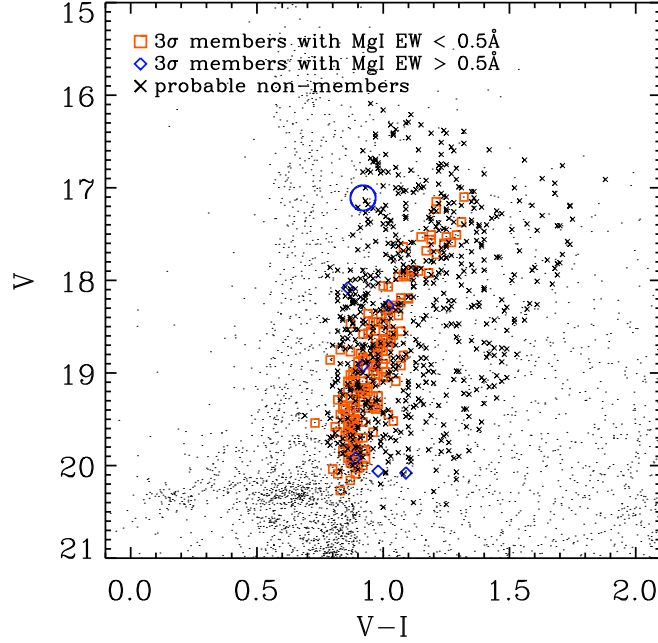


**Figure 6.** Colour-magnitude diagram of stellar objects for Sextans as obtained from INT/WFC and ESO/WFI imaging data (dots), with overlaid the targets of our VLT/FLAMES spectroscopic observations which passed our quality criteria. The squares indicate the probable Sextans members, the diamonds the stars that would have been classified as members from the  $3\sigma$  clipping but that have a too large MgIEW ( $> 0.5 \text{ \AA}$ ), the crosses indicate the stars with velocities outside the  $3\sigma$  range of selection. The star encircled has a discrepant location on the CMD with respect to the other Sextans members of all metallicities, and it is the outermost star in our sample with a projected radius of more than 2 deg from Sextans centre. We believe that this star is likely to be a contaminant as well.

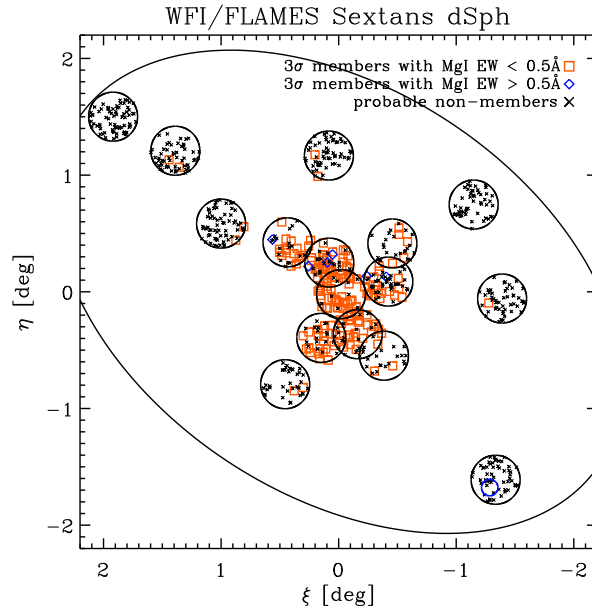


**Figure 7.** Location of the observed VLT/FLAMES fields (solid circles) and targets in Sextans (squares: probable members; diamonds: stars with velocities within the  $3\sigma$  range of selection but with too large MgIEW for giant stars; crosses: non-members with velocities outside the  $3\sigma$  range of selection). The small blue circle indicate the star with peculiar location on the CMD. The ellipse shows the nominal tidal radius (value from Irwin & Hatzidimitriou 1995).

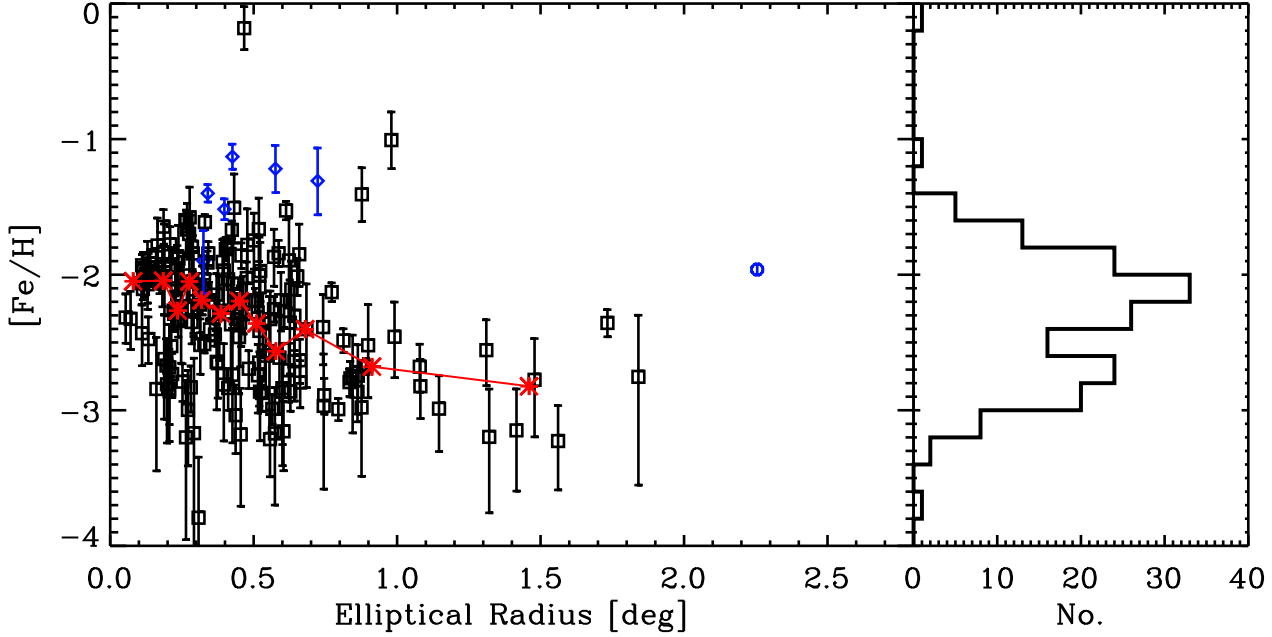


**Figure 8.** Left: Metallicity distribution as function of elliptical radius for the probable members of Sextans (squares with error-bars). The diamonds with error-bars show those stars whose velocities fall within the  $3\sigma$  range of membership, but that are likely non-members based on their large  $\text{MgIEW}$  ( $> 0.5 \text{ \AA}$ ). The small blue circle indicate the star with peculiar location on the CMD. Since the stars represented with the diamonds and the blue circle are likely non-members they will not be considered when deriving properties relative to Sextans. The red asterisks connected by a solid line represent a running median over 15 stars (except for the last point, which is over 9 stars). Right: Metallicity distribution for Sextans members (from the squares in right-handside panel).

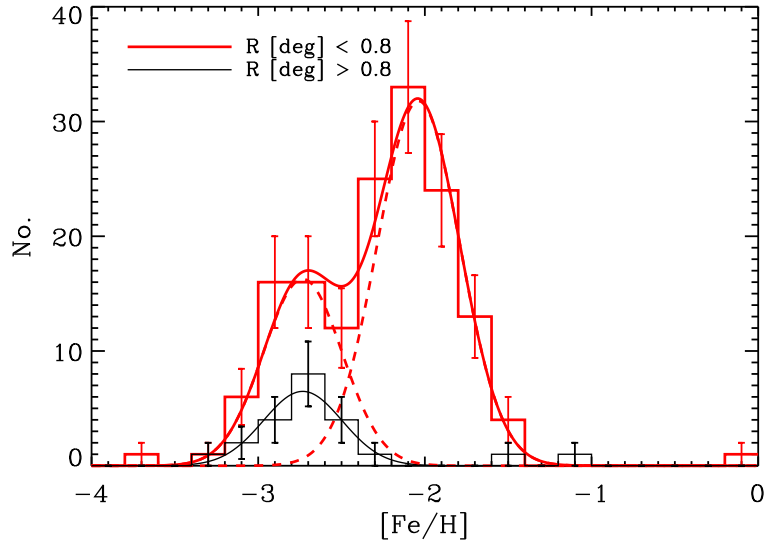


**Figure 9.** Metallicity distribution for Sextans probable members at projected radii  $R < 0.8 \text{ deg}$  (thick red histogram) and at  $R > 0.8 \text{ deg}$  (thin black histogram). The solid black thin line shows the Gaussian fit to the distribution at  $R > 0.8 \text{ deg}$ ; the thick solid red line shows the best fit to the distribution at  $R < 0.8 \text{ deg}$  for a sum of two Gaussians; the position of the central  $[\text{Fe}/\text{H}]$  and dispersion of one of the two Gaussian is kept constant to the values found for the distribution at  $R > 0.8 \text{ deg}$ . The dashed lines show the two Gaussians separately. The error-bars are Poissonian.

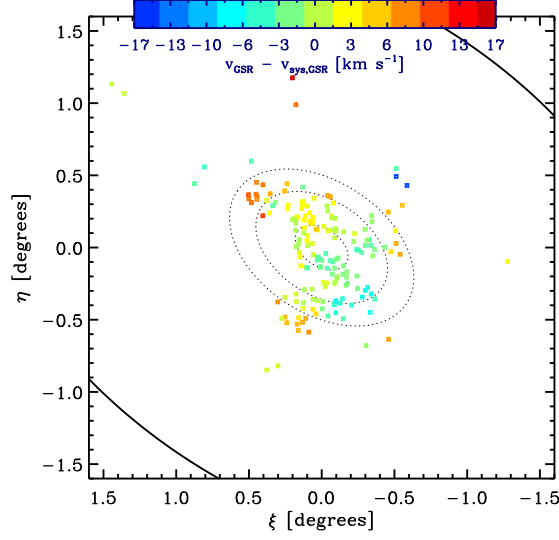


**Figure 10.** Velocity field for probable members to Sextans. The velocities are smoothed with a “median filter”, i.e. we associate to each star the median velocity of the stars located within a square of side 0.2 deg centred on the considered star; this smoothing is just for visual purposes and aims at reducing the velocity variations due to the dispersion of the galaxy. We use the velocities in the GSR frame to avoid spurious gradients introduced by the component of the Sun and LSR motions along the l.o.s. to Sextans. The colour bar gives the velocity scale. The dotted ellipses are placed at 0.2, 0.5, and 0.7 deg to give an idea of the distance scale. The solid ellipse shows the nominal tidal radius (from Irwin & Hatzidimitriou 1995).

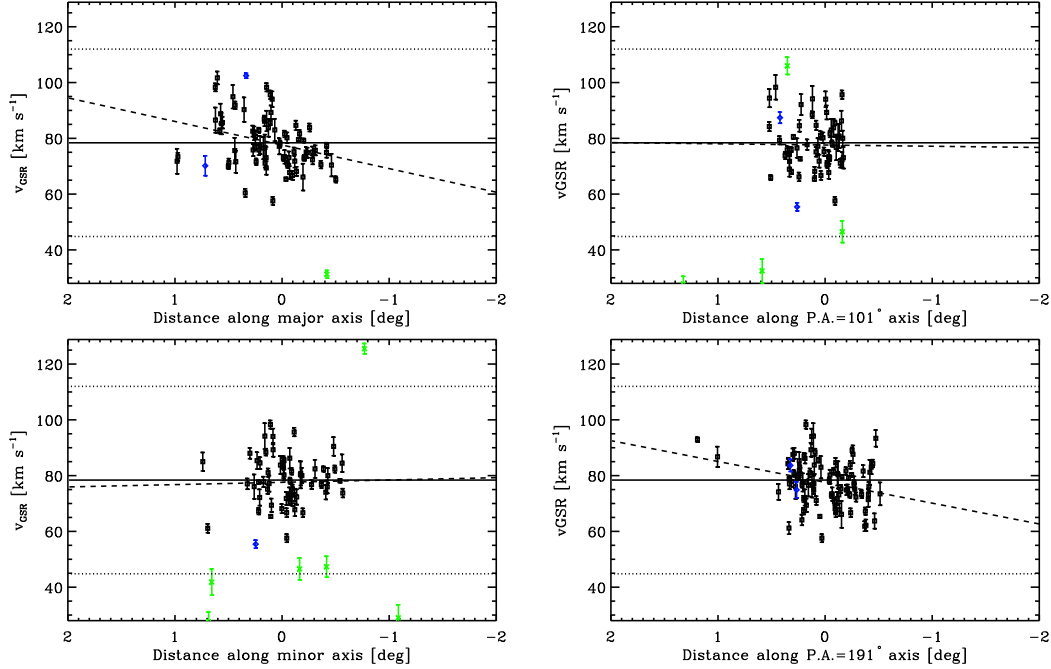


**Figure 11.**  $v_{\text{GSR}}$  for probable Sextans members versus distance along axes at P.A.=  $56^\circ$  (major axis),  $101^\circ$ ,  $146^\circ$  (minor axis),  $191^\circ$  for stars located within  $\pm 0.15^\circ$  from these axes (squares with error bars). The probable non-members within the same spatial region are shown as diamonds and crosses with error-bars (stars with velocity consistent with membership but with Mg I EW too large for giant stars and stars with velocity outside the  $3\sigma$  selection region, respectively). The solid line indicates the systemic velocity of Sextans; the dotted lines indicate a region in velocity of  $\pm 3\sigma$  from the systemic; the dashed line shows the best-fitting straight line to the data (see the text for the values of the best fit).

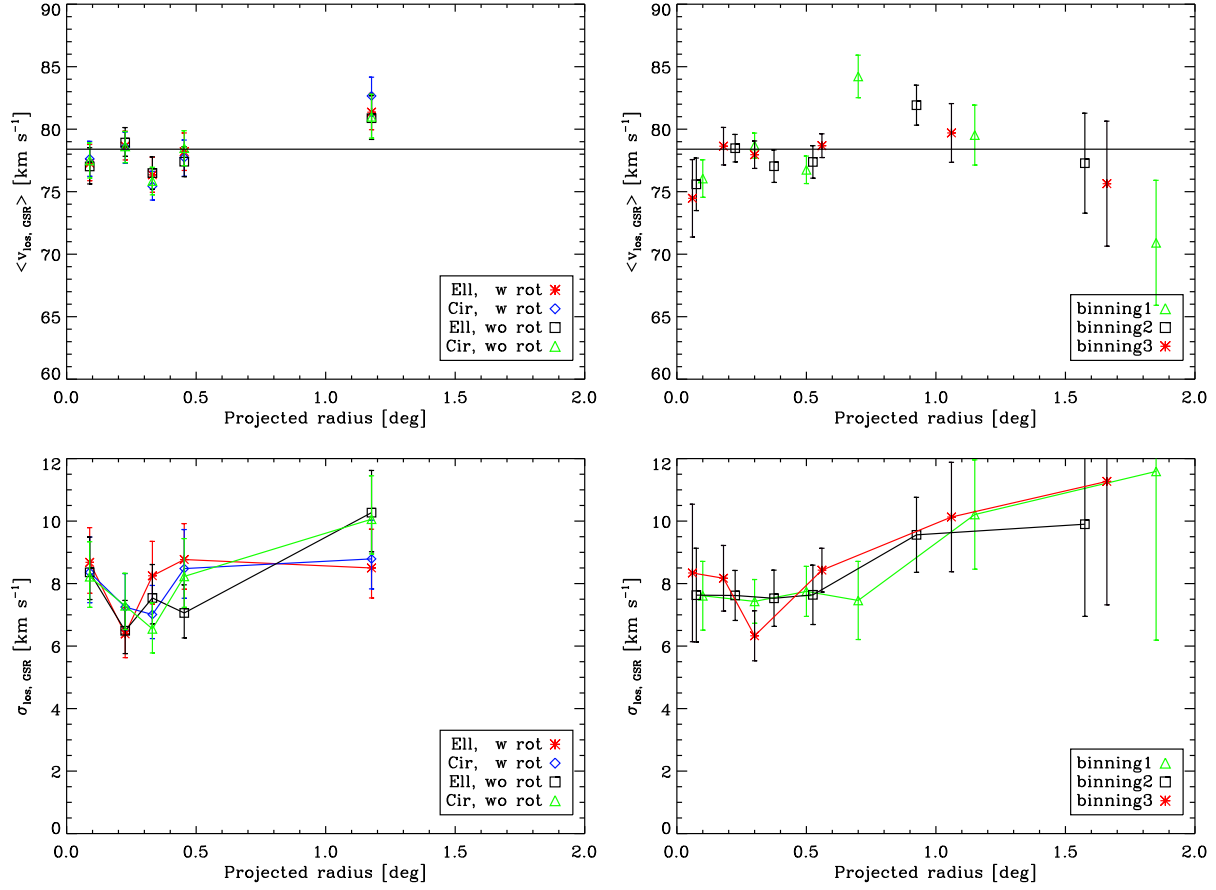


**Figure 12.** L.o.s. average velocity (top) and velocity dispersion profile (bottom) in GSR system for probable Sextans members versus projected radius. Left: profiles derived keeping the number of stars per bin approximately constant to 35 stars per bin; the profiles have been derived both when the velocity gradient is included (asterisks: elliptical binning; diamonds: circular binning) and when it is subtracted from the individual velocities (squares: elliptical binning; triangles: circular binning). Right: profiles derived for 3 different choices of binning with bins of increasing width with projected radius, in the case when the gradient is subtracted from the individual velocities and elliptical binning. The horizontal solid line in the top panel indicates the systemic velocity of Sextans.

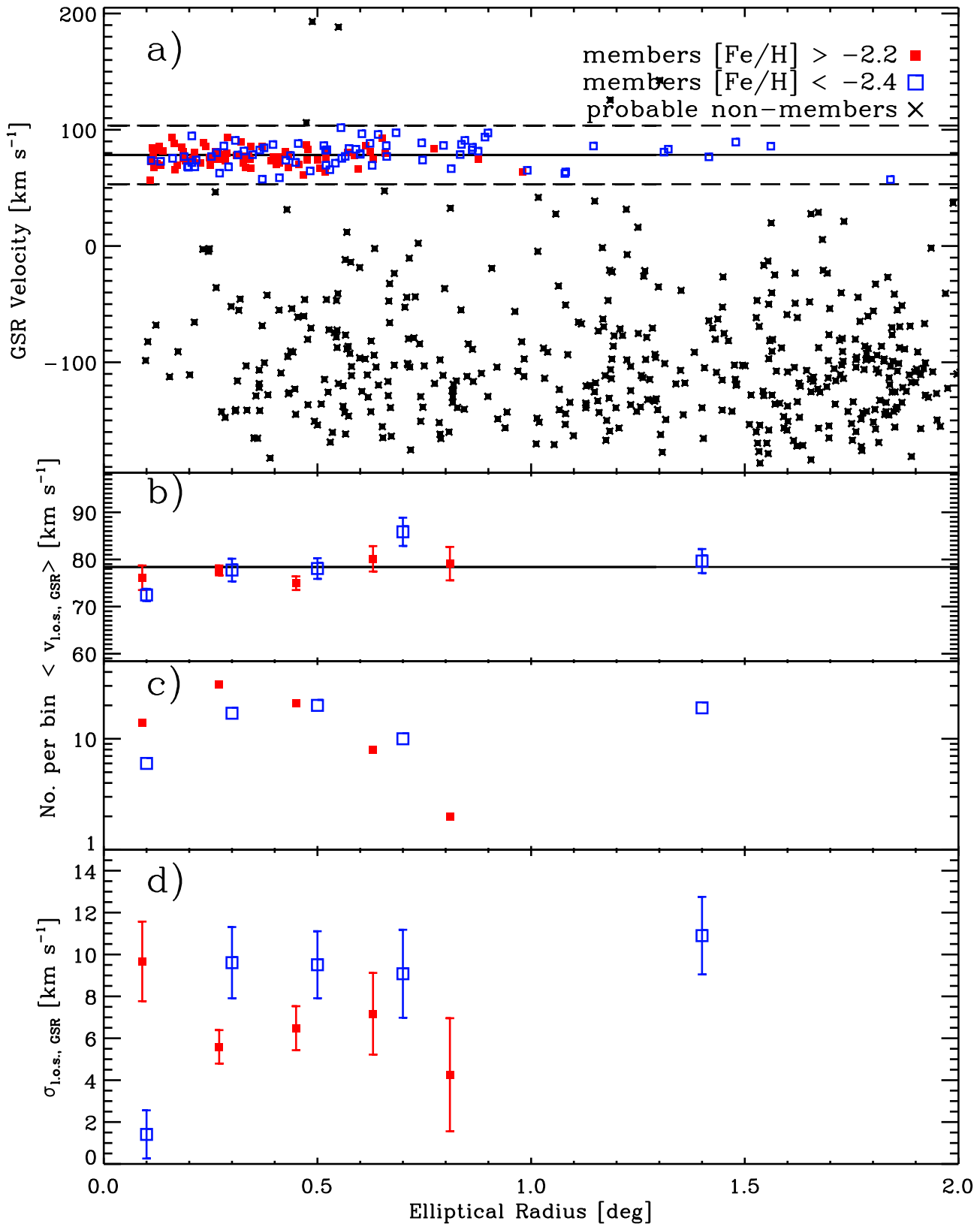


**Figure 13.** Kinematic properties for probable Sextans members more metal rich than  $[\text{Fe}/\text{H}] = -2.2$  (red filled squares) and more metal poor than  $[\text{Fe}/\text{H}] = -2.4$  (blue open squares). We show the variation of the rotation-subtracted GSR velocity versus elliptical radius (a); average rotation-subtracted GSR velocity (b); number of stars (c); velocity dispersion profile using rotation-subtracted GSR velocities (d). The solid horizontal line indicates the systemic velocity, the horizontal long-dashed lines show the region used for the  $3\sigma$  membership selection.



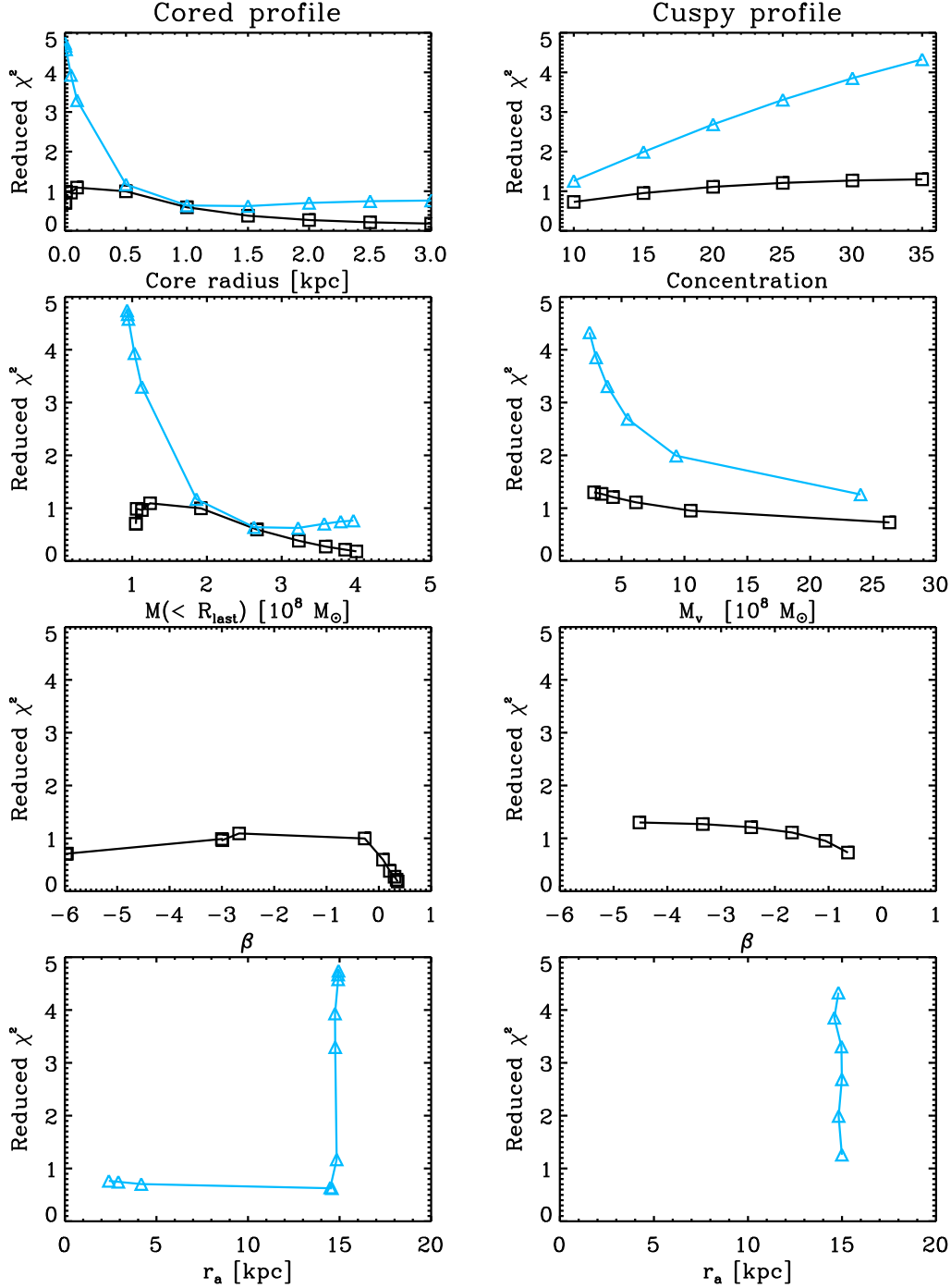


**Figure 14.** In this figure we summarize the results of the mass modelling when using the observed l.o.s. velocity dispersion profile derived with “Binning2” (left: cored dark matter profile; right: cuspy dark matter profile). From top to bottom we plot the reduced  $\chi^2$  values for the best fit model as a function of core radius (left) and concentration (right), mass within the last measured point at  $\sim 2.3$  kpc (left) and virial mass (right) both in units of  $10^8 M_\odot$ , velocity anisotropy in the hypothesis of constant anisotropy with radius, anisotropy radius in the hypothesis of velocity anisotropy following an Osipkov-Merritt profile. The black squares and cyan triangles show the results in the hypothesis of  $\beta = \text{const}$  and  $\beta = \beta_{\text{OM}}$ , respectively. For each of the core radius (concentration) values shown in the top left (right) panel, the models are optimized over the anisotropy and mass parameters. The quoted reduced  $\chi^2$  values are therefore the value of the  $\chi^2$  for the best fit model over 4 degrees of freedom.

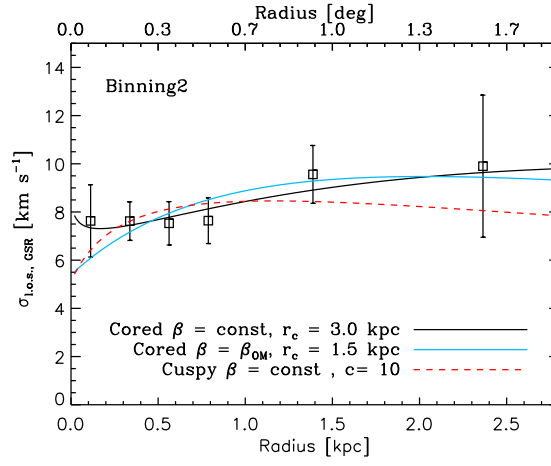


**Figure 15.** Observed l.o.s. velocity dispersion profile (squares with error-bars) overlaid on the best fit model for a cored profile with  $\beta$  constant (solid black line), a cored profile with  $\beta_{\text{OM}}$  (solid cyan line), cuspy profile with  $\beta$  constant (dashed line) for “Binning2”.

## REFERENCES

- Aoki W., Arimoto N., Sadakane K., Tolstoy E., Battaglia G., Jablonka P., Shetrone M., Letarte B., Irwin M., Hill V., Francois P., Venn K., Primas F., Helmi A., Kaufer A., Tafelmeyer M., Szeifert T., Babusiaux C., 2009, *A&A*, 502, 569
- Battaglia G., 2007, PhD thesis, Kapteyn Astronomical Institute, University of Groningen
- Battaglia G., Helmi A., Tolstoy E., Irwin M., Hill V., Jablonka P., 2008, *ApJ*
- Battaglia G., Irwin M., Tolstoy E., Hill V., Helmi A., Letarte B., Jablonka P., 2008, *MNRAS*
- Battaglia G., Tolstoy E., Helmi A., Irwin M. J., Letarte B., Jablonka P., Hill V., Venn K. A., Shetrone M. D., Arimoto N., Primas F., Kaufer A., Francois P., Szeifert T., Abel T., Sadakane K., 2006, *A&A*, 459, 423
- Bellazzini M., Ferraro F. R., Pancino E., 2001, *MNRAS*, 327, L15
- Binney J., Mamon G. A., 1982, *MNRAS*, 200, 361
- Binney J., Merrifield M., 1998, *Galactic astronomy. Galactic astronomy / James Binney and Michael Merrifield.* Princeton, NJ : Princeton University Press, 1998. (Princeton series in astrophysics) QB857 .B522 1998
- Binney J., Tremaine S., 1987, *Galactic dynamics.* Princeton, NJ, Princeton University Press, 1987, 747 p.
- Blecha A., North P., Royer F., Simond G., 2003, VLT-SPE-OGL-13730-0040
- Bullock J. S., Kolatt T. S., Sigad Y., Somerville R. S., Kravtsov A. V., Klypin A. A., Primack J. R., Dekel A., 2001, *MNRAS*, 321, 559
- Carretta E., Gratton R. G., 1997, 121, 95
- Cole A. A., Smecker-Hane T. A., Tolstoy E., Bosler T. L., Gallagher J. S., 2004, 347, 367
- Da Costa G. S., Hatzidimitriou D., Irwin M. J., McMahon R. G., 1991, *MNRAS*, 249, 473
- Dehnen W., Binney J. J., 1998, *MNRAS*, 298, 387
- Faria D., Feltzing S., Lundström I., Gilmore G., Wahlgren G. M., Ardeberg A., Linde P., 2007, *A&A*, 465, 357
- Fraternali F., Tolstoy E., Irwin M. J., Cole A. A., 2009, *A&A*, 499, 121
- Geha M., van der Marel R. P., Guhathakurta P., Gilbert K. M., Kalirai J., Kirby E. N., 2010, *ApJ*, 711, 361
- Geisler D., Sarajedini A., 1996, in Morrison H. L., Sarajedini A., eds, *Formation of the Galactic Halo...Inside and Out Vol. 92 of Astronomical Society of the Pacific Conference Series, Standard Giant Branches in the Washington System: Calibration and Application to the Draco, Ursa Minor and Sextans Dwarf Spheroidal Galaxies.* pp 524–
- Gilmore G., Wilkinson M. I., Wyse R. F. G., Kleya J. T., Koch A., Evans N. W., Grebel E. K., 2007, *ApJ*, 663, 948
- Gullieuszik M., Held E. V., Saviane I., Rizzi L., 2009, *A&A*, 500, 735
- Harbeck D., Grebel E. K., Holtzman J., Guhathakurta P., Brandner W., Geisler D., Sarajedini A., Dolphin A., Hurley-Keller D., Mateo M., 2001, *AJ*, 122, 3092
- Hargreaves J. C., Gilmore G., Irwin M. J., Carter D., 1994, *MNRAS*, 269, 957
- Helmi A., Irwin M. J., Tolstoy E., Battaglia G., Hill V., Jablonka P., Venn K., Shetrone M., Letarte B., Arimoto N., Abel T., Francois P., Kaufer A., Primas F., Sadakane K., Szeifert T., 2006, 651, L121
- Hoaglin D. C., Mosteller F., Tukey J. W., 1983, *Understanding robust and exploratory data analysis.* Wiley Series in Probability and Mathematical Statistics, New York: Wiley, 1983, edited by Hoaglin, David C.; Mosteller, Frederick; Tukey, John W.
- Illingworth G., 1976, *ApJ*, 204, 73
- Irwin M., Hatzidimitriou D., 1995, *MNRAS*, 277, 1354
- Irwin M. J., Bunclark P. S., Bridgeland M. T., McMahon R. G., 1990, *MNRAS*, 244, 16P
- Jing Y. P., 2000, *ApJ*, 535, 30
- Kleya J. T., Wilkinson M. I., Evans N. W., Gilmore G., 2004, *MNRAS*, 354, L66
- Kleya J. T., Wilkinson M. I., Gilmore G., Evans N. W., 2003, *ApJ*, 588, L21
- Klypin A., Zhao H., Somerville R. S., 2002, *ApJ*, 573, 597
- Koch A., Grebel E. K., Kleya J. T., Wilkinson M. I., Harbeck D. R., Gilmore G. F., Wyse R. F. G., Evans N. W., 2007, *AJ*, 133, 270
- Koch A., Grebel E. K., Wyse R. F. G., Kleya J. T., Wilkinson M. I., Harbeck D. R., Gilmore G. F., Evans N. W., 2006, 131, 895
- Koch A., Wilkinson M. I., Kleya J. T., Gilmore G. F., Grebel E. K., Mackey A. D., Evans N. W., Wyse R. F. G., 2007, *ApJ*, 657, 241
- Kormendy J., Fisher D. B., Cornell M. E., Bender R., 2009, *ApJS*, 182, 216
- Lee M. G., Park H. S., Park J.-H., Sohn Y.-J., Oh S. J., Yuk I.-S., Rey S.-C., Lee S.-G., Lee Y.-W., Kim H.-I., Han W., Park W.-K., Lee J. H., Jeon Y.-B., Kim S. C., 2003, *AJ*, 126, 2840
- Letarte B., Hill V., Jablonka P., Tolstoy E., François P., Meylan G., 2006, *A&A*, 453, 547
- Lewis G. F., Ibata R. A., Chapman S. C., McConnachie A., Irwin M. J., Tolstoy E., Tanvir N. R., 2007, *MNRAS*, 375, 1364
- Li Y., Helmi A., De Lucia G., Stoeck F., 2009, *MNRAS*, 397, L87
- Lokas E. L., 2009, *MNRAS*, 394, L102
- Lokas E. L., Mamon G. A., Prada F., 2005, *MNRAS*, 363, 918
- Mamon G. A., Lokas E. L., 2005, *MNRAS*, 363, 705
- Mateo M., Fischer P., Krzemiński W., 1995, *AJ*, 110, 2166
- Mateo M., Nemec J., Irwin M., McMahon R., 1991, *AJ*, 101, 892
- Mateo M., Olszewski E. W., Walker M. G., 2008, *ApJ*, 675, 201
- Mateo M. L., 1998, *ARA&A*, 36, 435
- Merritt D., 1985, *MNRAS*, 214, 25P
- Muñoz R. R., Majewski S. R., Johnston K. V., 2008, *ApJ*, 679, 346
- Navarro J. F., Frenk C. S., White S. D. M., 1996, *ApJ*, 462, 563
- Navarro J. F., Frenk C. S., White S. D. M., 1997, *ApJ*, 490, 493
- Oh K. S., Lin D. N. C., Aarseth S. J., 1995, *ApJ*, 442, 142
- Okamoto S., Arimoto N., Yamada Y., Onodera M., Tolstoy E., Irwin M., Helmi A., Battaglia G., Jablonka P., Hill V., Venn K., Shetrone M., Letarte B., Primas F., Francois P., Sadakane K., Kaufer A., Szeifert T., Abel T., 2008, in T. Kodama, T. Yamada, & K. Aoki ed., *Astronomical Society of the Pacific Conference Series Vol. 399 of As-*

tronomical Society of the Pacific Conference Series, The Star Formation History and Stellar Population Structures in the Sextans Dwarf Spheroidal Galaxy. pp 469–+

Osipkov L. P., 1979, *Soviet Astronomy Letters*, 5, 42

Pasquini L., Ávila G., Blecha A., Cacciari C., Cayatte V., Colless M., Damiani F., de Propris R. e. a., 2002, *The Messenger*, 110, 1

Pryor C., McClure R. D., Fletcher J. M., Hesser J. E., 1988, in J. E. Grindlay & A. G. D. Philip ed., *The Harlow-Shapley Symposium on Globular Cluster Systems in Galaxies Vol. 126 of IAU Symposium, A Survey of Globular Cluster Velocity Dispersions*. pp 661–+

Revaz Y., Jablonka P., Sawala T., Hill V., Letarte B., Irwin M., Battaglia G., Helmi A., Shetrone M. D., Tolstoy E., Venn K. A., 2009, *A&A*, 501, 189

Robin A. C., Reylé C., Derrière S., Picaud S., 2003, *A&A*, 409, 523

Rutledge G. A., Hesser J. E., Stetson P. B., Mateo M., Simard L., Bolte M., Friel E. D., Copin Y., 1997, 109, 883

Sales L. V., Navarro J. F., Abadi M. G., Steinmetz M., 2007, *MNRAS*, 379, 1475

Schlegel D. J., Finkbeiner D. P., Davis M., 1998, *ApJ*, 500, 525

Shetrone M. D., Côté P., Sargent W. L. W., 2001, *ApJ*, 548, 592

Starkenburg E., Hill V., Tolstoy E., González Hernández J. I., Irwin M., Helmi A., Battaglia G., Jablonka P., Tafelmeyer M., Shetrone M., Venn K., de Boer T., 2010, *A&A*, 513, A34+

Strigari L. E., 2010, *Advances in Astronomy*, 2010, 11

Strigari L. E., Bullock J. S., Kaplinghat M., Diemand J., Kuhlen M., Madau P., 2007, *ApJ*, 669, 676

Strigari L. E., Bullock J. S., Kaplinghat M., Simon J. D., Geha M., Willman B., Walker M. G., 2008, *Nature*, 454, 1096

Suntzeff N. B., Mateo M., Terndrup D. M., Olszewski E. W., Geisler D., Weller W., 1993, *ApJ*, 418, 208

Swaters R. A., Madore B. F., Trewheella M., 2000, *ApJ*, 531, L107

Tolstoy E., Hill V., Tosi M., 2009, *ARA&A*, 47, 371

Tolstoy E., Irwin M. J., Helmi A., Battaglia G., Jablonka P., Hill V., Venn K. A., Shetrone M. D., Letarte B., Cole A. A., Primas F., Francois P., Arimoto N., Sadakane K., Kaufer A., Szeifert T., Abel T., 2004, 617, L119

van den Bergh S., 2006, *AJ*, 131, 304

Walker M. G., Mateo M., Olszewski E. W., 2008, *ApJ*, 688, L75

Walker M. G., Mateo M., Olszewski E. W., 2009, *AJ*, 137, 3100

Walker M. G., Mateo M., Olszewski E. W., Gnedin O. Y., Wang X., Sen B., Woodroffe M., 2007, *ApJ*, 667, L53

Walker M. G., Mateo M., Olszewski E. W., Pal J. K., Sen B., Woodroffe M., 2006, *ApJ*, 642, L41

Walker M. G., Mateo M., Olszewski E. W., Peñarrubia J., Wyn Evans N., Gilmore G., 2009, *ApJ*, 704, 1274

Walker M. G., Mateo M., Olszewski E. W., Peñarrubia J., Wyn Evans N., Gilmore G., 2010, *ApJ*, 710, 886

Wechsler R. H., Bullock J. S., Primack J. R., Kravtsov A. V., Dekel A., 2002, *ApJ*, 568, 52

## APPENDIX: COMPARISON WITH WALKER ET AL. (2009)

We compare our dataset of objects with  $S/N \geq 10$  and velocity errors  $\leq 5 \text{ km s}^{-1}$  to the recent data-set of Walker et al. (2009) consisting of spectroscopic observations of 947 distinct targets along the line-of-sight to Sextans acquired with the Michigan/MIKE Fiber System ( $R=20000\text{--}25000$ ). These spectra cover the wavelength range  $5140\text{--}5180 \text{ \AA}$  including the magnesium triplet absorption feature which the authors use, together with calibrating globular clusters, to provide an estimate of  $[\text{Fe}/\text{H}]$  for the individual stars.

### Velocities

There are 141 overlapping individual stars with velocity determinations between our and Walker et al. (2009) samples, including probable members and non-members. In Fig. 16 (left) we compare the line-of-sight velocities for the stars overlapping between the two samples.

The agreement between the velocity determinations in the two data-sets is good: the weighted average velocity difference between the two samples is  $1.3 \pm 1.3 \text{ km s}^{-1}$ , with a scaled MAD of  $3.8 \text{ km s}^{-1}$  (corresponding to about an average velocity error of  $2.5 \text{ km s}^{-1}$  in each of the two datasets) and 1.4 for the distribution of velocity differences normalized by the errors. Overall the agreement is good, except for 5 stars, which have velocities consistent with membership to Sextans in our sample but heliocentric velocities below  $20 \text{ km s}^{-1}$  in the Walker et al. (2009) sample, which would classify them as clearly MW stars: the velocities of these differ by about  $250\text{--}300 \text{ km s}^{-1}$  between the two samples. All these stars have very reasonable  $S/N$  in our data and visual examination of the spectra of these 5 stars with discrepant velocities does not reveal any problem with the spectrum (i.e. CaT is in general visible enough to allow a reasonable velocity estimation with our routine). We find it unlikely that these may all be binary stars, but the reason for this discrepancy remains unclear.

Excluding these 5 stars does not significantly alter the quality of the comparison between the two samples, bringing some improvement in the average velocity difference between the two samples ( $0.41 \pm 0.44 \text{ km s}^{-1}$ ), while the scaled MAD remains almost unchanged.

### Metallicities

Since the  $[\text{Fe}/\text{H}]$  calibrations in both studies are based on different spectral features, a comparison between the  $[\text{Fe}/\text{H}]$  determinations of the individual stars is expected to be meaningful only when considering probable Sextans members, and not for the MW contaminants for which the luminosity correction for the dwarf stars is likely to be incorrect and different in the two studies. Walker et al. (2009) derive  $[\text{Fe}/\text{H}]$  measurements from a Mg index and place them on the Carretta & Gratton (1997) scale (their Eq. 7). The calibration of the spectral indexes to a  $[\text{Fe}/\text{H}]$  scale requires a correction for the V-magnitude of the stars, therefore the authors provided  $[\text{Fe}/\text{H}]$  values only for those Sextans stars in common between their sample and the photometric study of Lee et al. (2003), using the V-magnitudes derived in the latter work. This would result in 50 probable Sextans members

with  $[\text{Fe}/\text{H}]$  estimates in common between the two studies. In order to increase the number of stars available for comparison with our sample, we check that the V-magnitudes obtained from our photometry compares well to the determinations of Lee et al. (2003) for the same stars, and then use our V-magnitudes for those stars in common between our sample and Walker's but that did not have determinations from Lee et al. (2003); this gives an additional 44 probable members in common between the two samples. The results of the comparison are shown in the right panel of Fig. 16: in general the determinations from W09 yield higher values of  $[\text{Fe}/\text{H}]$  (more metal rich) and the  $[\text{Fe}/\text{H}]$  distribution appears much narrower. This effect was also highlighted by Walker et al. (2009) and the authors themselves advise against using the determinations from the Mg index as absolute values. The authors suggest that the Mg spectral index could be used as a relative indicator of metallicity. In Fig. 16 (right) we show that the metallicities from the Mg spectral index correspond to a narrower range than the more reliable CaT measurements, suggesting a limited use of the Mg index also for relative measurements. It appears also not possible to carry out a reliable calibration between  $[\text{Fe}/\text{H}]$  estimates from CaT and from Mg index because of the large scatter between the two quantities (Fig. 17).

The fact that the Mg index is not a good indicator of  $[\text{Fe}/\text{H}]$  prevents us from combining our sample of metallicities with those of Walker et al. (2009). However, such a merged data-set would be most helpful to considerably increase the size and coverage of both works.

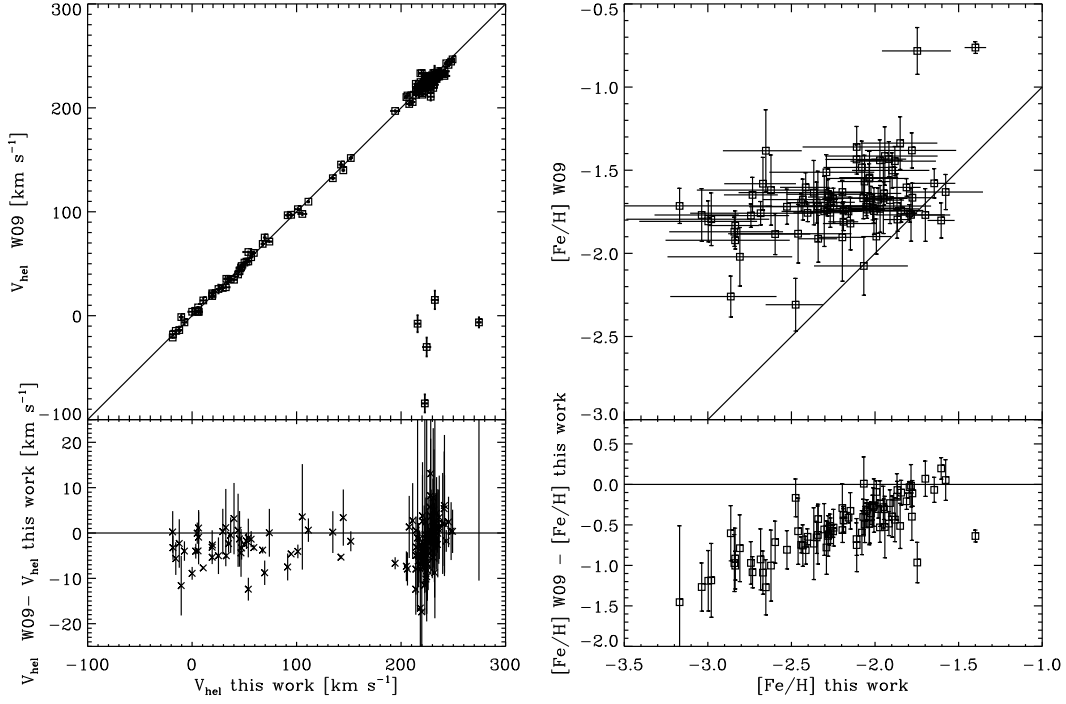


**Figure 16.** Comparison between overlapping stars between this work and Walker et al. (2009). The comparison for the velocity determinations is shown in the left panels (134 stars, both probable members and non-members), and for the  $[\text{Fe}/\text{H}]$  values in the right panels (94 stars, only probable members). The top panels show the direct comparison, with the solid line indicating the one-to-one relation; the bottom panels show the differences among the determinations as a function of the quantities derived in this work, with the solid line indicating a null difference.

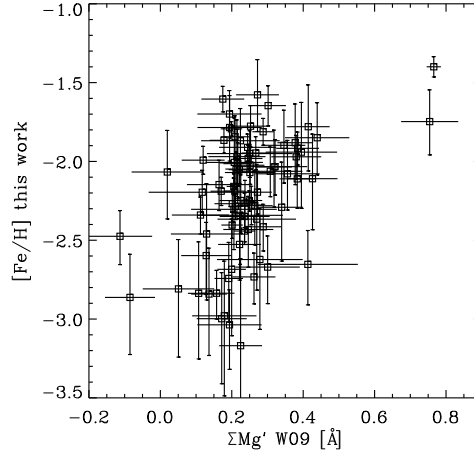


**Figure 17.**  $[\text{Fe}/\text{H}]$  values as determined in this work against determinations of the Mg spectral index from Walker et al. (2009) for 94 Sextans probable members which overlap between the two samples. Note the large range of  $[\text{Fe}/\text{H}]$  values corresponding to a narrow range in spectral index values.